Molecular Vision 2026; 32:281-306 <http://www.molvis.org/molvis/v32/281>
Received 1 November 2025 | Accepted 8 July 2026 | Published 10 July 2026

© 2026 Molecular Vision

A mutation in *Bicdl1* (BICD family-like cargo adaptor 1) leads to mild outer retina thinning and late retinal dysfunction in a mouse model.

Gizem Ulker-Yilmazer,[1] Dogan Can Kirman,[1] Tian Yu,[1] Emily R. Turpin,[1] Sangita Shrestha,[1] Seher Yuksel,[1] Yu-Guang He,[1] Sara Ludwig,[2] Ashwani Kumar,[3] Chao Xing,[3,4,5] Eva M.Y. Moresco,[2] Bruce A. Beutler,[2] Bogale Aredo,[1] Rafael L. Ufret-Vincenty[1]

(The first two authors contributed equally to this work.)

[1]Department of Ophthalmology, University of Texas Southwestern Medical Center, Dallas, TX; [2]Center for the Genetics of Host Defense, University of Texas Southwestern Medical Center, Dallas, TX; [3]McDermott Center for Human Growth and Development, University of Texas Southwestern Medical Center, Dallas, TX; [4]Department of Bioinformatics, University of Texas Southwestern Medical Center, Dallas, TX; [5]Department of Population and Data Sciences, University of Texas Southwestern Medical Center, Dallas, TX

Purpose: Both photoreceptors and the retinal pigment epithelium (RPE) are highly metabolically active cell types that require extensive molecular transport and adequate energy production to maintain their function. We tested the hypothesis that cargo adaptor protein Bicdl1 has a non-redundant role in retinal health.
Methods: Using an unbiased forward genetics approach, we identified an association between outer retinal thinning and a point mutation in *Bicdl1*. We generated *Bicdl1* KI (knock-in) mice carrying the same point mutation identified in the mutagenesis pipeline and characterized the resulting retinal phenotype using optical coherence tomography (OCT), fundus photography, histology, immunofluorescence, electroretinography, electron microscopy (EM), and transcriptomics.
Results: Analysis of OCT images and histology sections demonstrated a mild decrease in outer retinal thickness and rod outer segment thickness. We found an increased number of fundus spots in retinal photographs and an increased number of $Iba1^+$/$Tmem119^+$ cells on RPE flat mounts of *Bicdl1* KI mice. Electroretinography in aging mice showed a mild impairment in visual function, reflected by a reduction in a-wave amplitudes. EM revealed fewer RPE mitochondria in *Bicdl1* KI mice. To elucidate the mechanistic basis of the observed retinal degeneration, transcriptomic studies were conducted, which suggested an association between low *Bicdl1* expression and increased oxidative phosphorylation in photoreceptors.
Conclusion: Despite the expression of many cargo adaptor proteins and dynein activators in the retina, we identified a novel non-redundant role of *Bicdl1* in retinal homeostasis. Pathway analysis of transcriptomic data suggested that *Bicdl1* deficiency may affect energy metabolism.

Photoreceptors are well-differentiated neuronal cells with unique functions that play a critical role in visual perception. The outer segments of rod photoreceptors contain numerous discs where phototransduction occurs. Maintaining this complex structure requires extensive transport of molecules. Any defect in intracellular trafficking may cause disrupted recycling of visual proteins, inadequate outer segment renewal, and suboptimal function. Intracellular transport mechanisms are also essential for the complex metabolic processes orchestrated by the retinal pigment epithelium (RPE). In this work, using chemical mutagenesis and a forward genetic screening pipeline in mice, we identified a mutation in *Bicdl1* (BICD family-like cargo adaptor 1, *Bicdr1*, *Ccdc64*) that was associated with outer retinal abnormalities. This is noteworthy given the expression of a large number of proteins implicated in intracellular transport in photoreceptors and the RPE, suggesting potential for significant functional redundancy.

Cargo adaptor proteins link cargo molecules to intracellular motor proteins, enabling their transport within the cell. They are selective for specific cargoes and specific motors. They can activate motor proteins and even modulate the force generated by the transport complex, thereby influencing the direction of transport. Several cargo adaptor proteins, including Bicd2 (bicaudal D cargo adaptor 2), Bicdl1 (BICD family-like cargo adaptor 1), Hook2 (hook microtubule tethering protein 2), and Hook3 (hook microtubule tethering protein 3), are involved in the transport of Golgi-derived

Correspondence to: Rafael Ufret-Vincenty, Department of Ophthalmology, University of Texas Southwestern Medical Center, 5323 Harry Hines Blvd, Dallas, TX, 75390**;** email: Rafael.Ufret-Vincenty@UTSouthwestern.edu

vesicles, which is important for the proper distribution of cargoes [1,2]. Bicdl1 has a coiled-coil N-terminal domain, which interacts with dynein and dynactin. It mediates the attachment of cargoes to dynein, thereby facilitating their transport in the retrograde direction (towards the minus terminus of microtubules) [3,4].

In photoreceptors, the basal body, a specialized centrosome at the base of the cilium connecting the inner and outer segments, serves as a microtubule-organizing center and anchors the minus ends of microtubules. The transport of cargoes from the photoreceptor cell body to the outer segment on microtubules involves first retrograde transport (from the cell body towards the basal body by dynein- 1) followed by anterograde transport (from the basal body towards the outer segment by kinesin- 2), underscoring the importance of both dynein and kinesin for the maintenance of outer segment structure and function [5-10]. BICD family cargo adaptor proteins facilitate attachment of dynein to Rab6, which is an important regulator of post-Golgi traffic, particularly in the nervous system [11-13], helping transport the vesicles from the Golgi towards the basal body (minus end of microtubules) [3,14-16].

Given the importance of cargo adaptor proteins in the complex organization of the photoreceptor transport system and our findings from the mutagenesis screen, we hypothesized that Bicdl1 may have a role in outer retinal health that cannot be entirely compensated by other adaptor proteins. Thus, we endeavored to generate and characterize mice with a replacement allele containing the identified mutation in this gene using CRISPR technology. We provide evidence of mild outer nuclear layer (ONL) thickness and photoreceptor outer segment thinning, significant accumulation of fundus spots and subretinal Iba1$^+$/Tmem119$^+$ cells. With aging, there was also evidence of a mild decrease in visual function. We also show transcriptomic data suggesting that, beyond its likely role in intracellular transport, *Bicdl1* may have an impact (direct or indirect) on oxidative phosphorylation and energy metabolism. If confirmed in future studies, this could be consistent with a connection between Bicdl1, intracellular transport, and oxygen metabolism in photoreceptors.

METHODS

Animals: All *Bicdl1* KI (*Bicdl1* knock-in) and wild-type (WT) male and female mice used in this study were on a C57BL/6J background. The number and ages of mice used are indicated for each experiment. All animals were maintained in a barrier animal facility at the University of Texas Southwestern Medical Center (UTSW Medical Center) on a 12-h -on/12-h -off light cycle and had free access to food and water. Before all procedures, the mice were anesthetized by intraperitoneal (IP) injection of a ketamine-xylazine cocktail (100 mg/kg - 5 mg/kg) and the eyes were dilated with a mixture (3:1) of tropicamide 1% solution (Alcon Laboratories, Inc. Fort Worth, TX) and phenylephrine hydrochloride 2.5% solution (Alcon, Inc. Lake Forest, IL). In the forward genetics pipeline, N-ethyl-N-nitrosourea (ENU) was used to induce random mutations in C57BL/6 founder male mice, which were then bred to C57BL/6J females (see below). *Bicdl1* knock in (KI) mice were generated using a CRISPR-Cas9 genome editing technique (details below). The study protocols and procedures were approved by the UTSW Medical Center Institutional Animal Care and Use Committee (IACUC, animal protocol # 2015-G100937). We followed all guidelines released by the National Institutes of Health (NIH) and the Association for Research in Vision and Ophthalmology (ARVO) for animal care and animal use in ophthalmic and vision research.

Forward genetic pipeline: ENU mutagenesis and whole-exome sequencing: In our forward genetic pipeline, for each pedigree, we used ENU to induce random mutations in a C57BL/6J founder male mouse (generation 0, G0). The founder was bred with C57BL/6J females to produce G1 mice. Whole-exome sequencing (WES) was then performed in male G1 mice to identify all exonic mutations. These G1 males were then crossed with C57BL/6J females to generate G2, and G2 females were backcrossed with G1 males to generate G3 mice (Figure 1B in Wang et al.) [17]. To establish zygosity in G2/G3 mice, genotyping was performed at each of the mutated loci identified in G1 mice. Optical coherence tomography (OCT) imaging was then used to screen G2 and G3 mice for retinal pathology (Appendix 1). Linkage Analyzer software was then used to correlate the magnitude of quantitative OCT phenotypes with the genotype at each mutation site for all mice in the pedigree [17-21]. The output of this automated mapping is a Manhattan plot of genotype-phenotype associations. In the Manhattan plot, $-\log_{10}$ p values (y-axis) for an association to a given phenotype are plotted versus the chromosomal positions of each mutations (x-axis) that had been identified in the G1 founders of each pedigree (Figure 1). In these plots, mice homozygous for the reference or WT allele are referred to as REF, mice heterozygous for the reference allele and variant allele are referred to as HET, and mice homozygous for variant or mutant allele are referred to as VAR. Mice that had not undergone mutagenesis (naive C57BL/6J mice) are referred to as WT (Figure 1).

Generation of Bicdl1 KI mice using the CRISPR-Cas9 system: For easy reference, we arbitrarily named the mutated *Bicdl1* allele identified in the mutagenesis pipeline the "*bargain* allele". CRISPR-Cas9 technology was used to generate *Bicdl1*

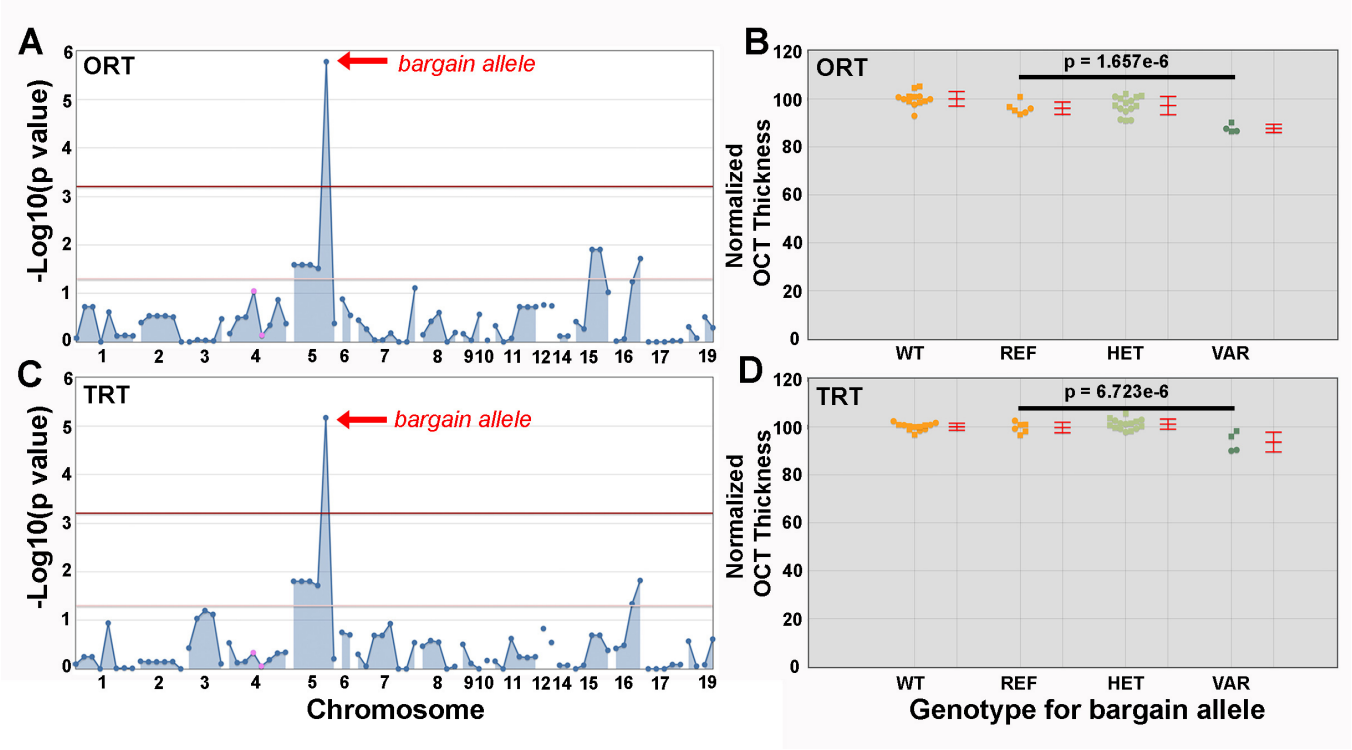

Figure 1. Association between the bargain allele of *Bicdl1* and thinning of the outer retina identified in a forward genetic screen in mice. Male C57BL/6J mice were mutagenized using ENU, and induced mutations were transmitted by breeding to third-generation (G3) descendants, which were screened for phenotypes. OCT imaging was used to screen the G3 mice. **A**, **C**: Linkage analyzer software was used to analyze gene-phenotype associations, resulting in Manhattan plots in which the x-axis represents chromosome numbers, while the y-axis indicates the strength of the association between each mutation (blue dots) and a given OCT parameter. ORT is shown in (**A**), TRT is shown in (**C**). One mutation (in *the bargain* allele) is significantly associated with thinning in ORT and TRT (p-values = $1.657e^{-6}$ and $6.723e^{-6}$, respectively). Two horizontal lines are shown: the lower and lighter line represents a p-value of 0.05, while the higher and darker line shows the threshold of significance after Bonferroni correction. **B**, **D**: Analysis of the screening data shows statistically significant thinning in ORT and TRT in only 4 mice, which have *Bicdl1* homozygote mutation, suggesting a recessive mode of inheritance. The graphics display the normalized ORT and TRT thicknesses as means ± SD across different groups of mice at 19-29 weeks of age. WT: wild type (non-mutagenized) mice (**B**, **D**; n = 13), REF: mice homozygous for the reference (wild type) sequence of *Bicdl1* (B, D; n = 6), HET: mice heterozygous for the *Bicdl1* mutation (**B**, **D**; n = 15), VAR: mice homozygous for the *Bicdl1* mutation (**B**, **D**; n = 4). ORT: outer retinal thickness, TRT: total retinal thickness.

KI mice expressing a replacement allele that precisely replicates the *bargain* allele (Appendix 2). This allele contains a single base substitution of guanine to adenine at coordinate 115,808,212 bp of mouse chromosome 5 (Genome Reference Consortium Mouse Build 39), corresponding to the first nucleotide of *Bicdl1* intron 4 (transcript variant 1 [NCBI reference sequence NM_001080808]; genomic sequence context: 5′-aaagacctacagGtactgggcagagaggct-3′, mutation site in uppercase). For both the *bargain* allele and the CRISPR-generated replacement allele, the predicted translation is a null protein product. Specifically, a single base pair substitution affecting a cryptic splicing site in intron 4 results in the insertion of 45 nucleotides from intron 4, leading to a shifted protein product beginning after amino acid 306 of the protein (which is normally 577 amino acids in length), and terminating after the inclusion of eight aberrant amino acids.

Bicdl1 KI mice harboring a replacement allele identical to the bargain allele (Appendix 2); mutated G to A at the splice donor site at coordinate 115,670,153 of GRCm38) on a C57BL/6J background were generated using CRISPR-Cas9 reagents at the Transgenic Center of UTSW Medical Center. The position of the G base to be mutated is 1nt from the 3′ end of exon 4 (ENSMUST00000055408.13 *Bicdl1*-201). The single guide RNA (sgRNA) sequence used was 5′TGA CAA AGA CCT ACA GGT ACT GG 3′. The guide was selected using the CRISPOR Design Tool. crRNA and tracRNA were annealed and mixed with Cas9 protein to form a ribonucleotide protein complex (RNP). The HDR template was 158nt with a silent mutation at the PAM site (TGG to TCG) to prevent the gRNA from cutting back the HDR knock-in template. The sequence of the HDR template was: 5′-CTG GAG CAT CGG CTC AGC GCC ACC TTG GAG GAG AAT

GAC CTG CTT CAA GGG ACT GTG GAG GAG CTG CAG GAC CGG GTG CTG ATC CTA GAA AGG CAG GGC CAT GAC AAA GAC CTA CAG ATA CTC GGC AGA GAG GCT ACT GCA TAG AGC TAG GGC CAG AC-3′.

All reagents were synthesized by Integrated DNA Technologies (IDT; Coralville, IA). The mix of CRISPR reagents, RNP complex, and HDR template was delivered into the cytoplasm of fertilized one-cell eggs isolated from superovulated females via cytoplasmic injection or electroporation using a NEPA21 electroporator (Nepa Gene Co., Ltd., Chiba, Japan), with a concentration range of 50- 400 ng for Cas9 protein, gRNA, and HDR template. The surviving eggs were transferred into the oviducts of day 0.5 pseudo-pregnant recipient ICR females (Envigo, Indianapolis, IN) to produce putative founder mice. To generate the *Bicdl1* KI line, we first crossed a *Bicdl1* KI founder male mouse with a female C57BL/6J mouse. We then crossed the resulting Het females with male C57BL/6J mice again to generate F2 pups. After this, we used a Het × Het breeding approach to generate *Bicdl1* WT and KI mice.

OCT acquisition and retinal thickness analysis: Mice were anesthetized one at a time, and the pupils were dilated before each experiment. GenTeal gel (Novartis, East Hanover, NJ) was applied to each eye to prevent corneal dryness. A Micron-OCT2 system (Phoenix-Micron Inc., Bend, OR) was used to acquire in vivo image-guided OCT images of both eyes of *Bicdl1* KI mice and WT littermates. After gently contacting the gel-covered cornea with the camera eyepiece and centering the fundus image on the optic nerve head (ONH), we focused on the retina to acquire a B-scan. We obtained a half-size horizontal line scan superior to the ONH at a distance of two disc diameters from the center of the ONH. Total retinal thickness (TRT, measured from Bruch's membrane to internal limiting membrane), outer nuclear layer (ONL) thickness, inner nuclear layer (INL), ganglion cell complex (GCC; top of the internal limiting membrane [ILM] to the top of the INL), and outermost retinal thickness (ORT, measured from Bruch's membrane to external limiting membrane) were obtained from analysis of each OCT image using ImageJ (NIH, Bethesda, MD) as described previously [21,22]. For each parameter, three measurements were taken: one at the center of the OCT image and two at distances of 100 microns on either side of the center. These three measurements were averaged for statistical comparisons between *Bicdl1* WT and KI mice. The number of mice used at different age groups is summarized as follows: 3-week-old (n = 7 WT and 5 KI), 2-month-old (n = 16 WT and 20 KI), 4-month-old (n = 16 WT and 17 KI), 6-month-old (n = 14 WT and 17 KI), 9-month-old (n = 19 WT and 19 KI), 12-month-old (n = 9 WT and 10 KI), and 15-month-old (n = 8 WT and 8 KI) per group.

Fundus photography and fundus spot grading: A Micron IV Retinal Imaging Microscope (Phoenix-Micron Inc., Bend, OR) was used to take color fundus images of both *Bicdl1* WT and KI mice, as previously described [19,21]. Fundus photography and fundus spot grading were obtained at the following ages: 2-month-old (n = 16 WT and 20 KI), 4-month-old (n = 15 WT and 17 KI), 6-month-old (n = 10 WT and 14 KI), 9-month-old (n = 10 WT and 9 KI) and 15-month-old (n = 8 WT and 8 KI). The fundus photos were graded for the accumulation of white/yellow fundus spots using a modified version of a previously described grading system [20,21]. The scale is as follows: Grade 0: no spots, grade 1: 1-3 spots, grade 2: 4-10 spots, grade 3: 11 spots - up to a quarter of retina covered with spots, grade 4: up to half of the retina covered with spots, grade 5: more than half of the retina covered with spots. A score is recorded for each eye, and the scores from both eyes are added to give the final mouse score.

A separate Spectralis® OCT (Heidelberg Engineering, Heidelberg, Germany) was used to examine the anatomical correlate for fundus spots. Images were acquired according to the manufacturer protocols.

Preparation of retinal sections for histology, TUNEL assay, and immunohistochemistry: To prepare histological specimens, we used a modified freeze-substitution protocol [23], which helped us preserve the retinal anatomy and cellular morphology in retinal sections. Mice were anesthetized by IP injection of a ketamine/xylazine cocktail, and their left eyes were enucleated and immediately fresh-frozen in liquid nitrogen-cooled isopentane. The frozen eye samples were transferred to a pre-cooled freeze substitution solution of methanol 97%/ acetic acid 3% (v/v) and stored in a −80 °C freezer for at least 48 h. The eyes were gradually warmed to room temperature, transferred to 100% ethanol, and submitted to the UTSW Medical Center Histo Pathology Core for paraffin embedding using routine techniques. Retinal cross sections (5 µm) were prepared for hematoxylin/eosin (H&E) staining, terminal deoxynucleotidyl transferase-mediated UTP end labeling (TUNEL) assay, and immunohistochemistry staining with caspase-3, rhodopsin, cone arrestin, and Iba1.

H&E staining was performed on mouse sagittal brain sections and retinal cross-sections using standard automated stainer procedures. Briefly, following appropriate fixation for each tissue, samples were paraffin-processed, embedded, and sectioned by members of the UT Southwestern Histo Pathology Core. Paraffin sections were prepared concomitantly and examined by dark-field microscopy. Sections were

stained for routine histopathologic evaluation by regressive H&E on a Sakura Prisma Plus x-y-z robotic stainer (Sakura Finetek USA, Inc., Torrance, CA) using Leica Selectech reagents (Hematoxylin 560 and Alcoholic Eosin Y 515, Leica Microsystems, Wetzlar, Germany). The H&E sections were imaged using a 20x objective lens (NA 1.0) on both sides of the ONH using a Leica DM2000 Upright Compound microscope (Leica Microsystems). The ONL thickness (in micrometers) and number of nuclei per ONL column (average of three columns) on the H&E images were measured at 500 µm intervals on both sides of the ONH (starting 300 µm from the edge of the ONH) using ImageJ.

The TUNEL assay was performed using the DeadEnd Fluorometric TUNEL system (Appendix 3) following the supplied protocol and previously published work [24]. Images were acquired using a Leica TCS SP8 confocal laser scanning microscope (Leica Microsystems) with a 25x objective lens (NA 1.0). The TUNEL-positive cells were quantified as the total number of TUNEL$^+$ cells per mouse on the acquired images.

For caspase-3 staining, the retinal sections were deparaffinized and subjected to heat-induced epitope retrieval in citrate buffer (pH 6.0) at 95°C for 20 min. Following blocking of endogenous peroxidases using 3% hydrogen peroxidase and secondary antibody host-serum affinity using 5% normal goat serum (S-1000; Vector Laboratories, Newark, CA), sections were incubated at 4 °C overnight with a rabbit polyclonal antibody against cleaved caspase-3 (Appendix 3). Detection involved incubating the sections with a biotinylated secondary goat anti-rabbit IgG (H+L) (Appendix 3), and amplification with avidin-biotin complex and streptavidin peroxidase (SA-5004-1; Vector Laboratories). Visualization was performed using 3,3′-diaminobenzidine (DAB, Appendix 3), followed by nuclear counterstaining with hematoxylin. Images were acquired using a Keyence BZ-X1000 microscope (Keyence Corporation, Osaka, Japan) with a 20x objective lens (NA 0.75) and the caspase-3-positive cells were quantified.

Rhodopsin staining was performed on 9-month-old (n = 4 WT and 5 KI) and 19-month-old *Bicdl1* (n = 5 WT and 5 KI) mice. Cone arrestin and microglia Iba1 staining were performed on 19-month-old *Bicdl1* (n = 5 WT and 5 KI) mice. The additional paraffin-embedded retinal sections were deparaffinized, and antigen retrieval was performed using the heat-induced epitope retrieval (HIER) method [25] by heating in citrate buffer (pH 6.0) in a 95°C water bath for 30 minutes. The sections were then blocked and incubated overnight with anti-Rhodopsin or anti-cone arrestin antibody, followed by an appropriate secondary antibody (Appendix 3). DAPI was used for nuclear counterstaining. All sections were imaged using a 25x objective lens (NA 1.0) on a Leica TCS SP8 confocal laser scanning microscope (Leica Microsystems). Images of rhodopsin-stained midperipheral retina were measured on both sides of the ONH. The total area of rhodopsin staining was measured in ImageJ and divided by the total length of the retina in every image, thus providing a measure of the average thickness of the rhodopsin staining over the entire section. We report values normalized to WT. Cone arrestin-stained images were taken at the central region, mid-periphery, and periphery on both sides of the ONH. In sum, a total of 6 fields were imaged for each mouse (three antero-posterior regions/side x 2 fields/region). For analysis, fields were grouped according to retinal region. Specifically, two peripheral fields were captured per eye (one per side), and with five eyes from five individual mice per experimental group, a total of ten peripheral fields were analyzed for each mouse line (similar for the central and midperipheral fields). We counted all cone-arrestin+ cells in each field. Retinal sections were examined for Iba1+ subretinal microglia and imaged with the same microscope and settings.

RPE and retina flat mount preparation for microglia/macrophage staining and analysis: RPE and retina flat mounts were prepared from 9- and 15-month-old *Bicdl1* WT and KI mice (n = 3 per group per age). After anesthesia via IP injection of a ketamine-xylazine cocktail, both eyes were enucleated and fixed in 4% paraformaldehyde (PFA) for 2 h. The fixed eyes were then dissected to remove the anterior segment (cornea, iris, and lens) and the retina was separated from the RPE-choroid-sclera. Both retinal and RPE-choroid-sclera flat mounts (hereafter referred to as RPE flat mounts) were prepared separately by making four radial cuts in the tissues, which were then flat-mounted on glass slides for immunostaining, as described previously [20,23]. In brief, the fixed retinal and RPE flat mounts were blocked in 5% donkey serum (v/v) with 0.3% Triton X-100 (v/v) & 0.2% bovine serum albumin (BSA) and 5% BSA (w/v) with 0.3% Triton X-100 (v/v), respectively, and then stained with anti-Iba1 (pan-microglia/macrophage marker), anti-Tmem119 (resident microglia-specific marker), and anti-CCR2 (marker for infiltrating monocyte-derived macrophages) primary antibodies followed by appropriate secondary antibodies (Appendix 3). A laser confocal microscope (see above) was used to image the paracentral and mid-peripheral regions in each of the four quadrants of each RPE flat mount. The images were analyzed using ImageJ, and the numbers of Iba1$^+$ or Tmem119$^+$ cells were counted separately in the paracentral and mid-peripheral regions of each RPE flat mount. The cell counts from these two regions were obtained for each eye and

statistically compared between *Bicdl1* WT and KI groups (n = 6 RPE flat mount per group).

Electron microscopy (EM): The right eyes of 9-month-old mice (n = 3 WT and 4 KI) were collected for transmission electron microscopy. The samples were collected after the mice were deeply anesthetized by IP injection of ketamine-xylazine cocktail and processed for EM, as described before [18]. Briefly, enucleated eyes were fixed in 2% glutaraldehyde and 2% PFA in 0.2 M cacodylate buffer (v/v). After fixation, the cornea and lens were removed, and the resulting posterior cup was trimmed for EM processing. Then, 70 nm thin sections were cut and stained with 2% aqueous uranyl acetate/lead citrate (v/v) and imaged with a JEOL 1200EX II transmission electron microscope (JEOL USA, Inc., Peabody, MA) at the UTSW Medical Center Electron Microscopy Core. EM fields were imaged in a masked and standardized fashion (the whole sample was scanned, and every other EM field was photographed). Thickness measurements were obtained for Bruch's membrane (BM), RPE basal infoldings, RPE cell body (excluding the microvilli), and from the bottom of the BM to the top of the RPE on each EM image at three equally spaced points using ImageJ. The average of these three measurements for each EM was reported for each parameter. The number of mitochondria in the apical and basal halves of RPE cells was also counted on each EM image.

Single-cell RNA sequencing (scRNA-seq) analysis and bulk RNA sequencing (bulk RNA-seq) confirmation: We extracted *Bicdl1* expression in 90-day-old C57BL/6J retina from a publicly available scRNA-seq dataset deposited by Li et. al. [26], under GEO accession # GSE243413 (WT_P90 mouse retina, GEO accession # GSM7785354). Cells in the rod photoreceptor cluster were categorized as being high *Bicdl1* expressors ("*Bicdl1*-hi", expression >2.5), medium expressors ("*Bicdl1*-med", expression between 1.5 and 2.5), or low expressors ("*Bicdl1*-lo", expression >0 and <1.5). Ingenuity pathway analysis (IPA) was performed by comparing *Bicdl1*-hi with *Bicdl1*-lo cells. For confirmation purposes, bulk RNA-seq was done following our published protocol [19,21]. Briefly, retinas from deeply anesthetized 9-week-old *Bicdl1* WT and KI mice (n = 4 per group) were collected. Three retinas (obtained from three different mice) were pooled to prepare each bulk RNA-seq sample. For each group we prepared 4 different pooled samples for total RNA isolation using a miRNeasy Tissue/Cells Advanced Micro Kit (Cat# 217684, Qiagen, Germantown, MD) according to the protocol supplied with the kit. After checking sample quality control, 1 µg total RNA/sample was submitted to the Next Generation Sequencing Core at UTSW Medical Center for bulk RNA-seq and pathway analysis.

Pathway analysis for both the scRNA-seq and the bulk RNA-seq data was performed using IPA on a set of differentially expressed genes meeting statistical cutoffs of p-value <0.05, and $\log_2$FC > 0.58 (~ fold change >1.5). After applying filters ($p < 0.001$, $|Z\text{-score}| > 2$, and ratio > 0.15), the top upregulated and downregulated pathways (up to 20 for each direction, if available) were graphed using dot plots. Only five downregulated pathways met the criteria in each of the data sets (bulk RNA-seq and scRNA-seq). Thus, a total of 25 pathways were selected for each dataset (green highlights in Appendix 4 and Appendix 5). Violin plots were generated using the VlnPlot module in Seurat. Meanwhile, the volcano plots were generated using an EnhancedVolcano package in R.

Electroretinography (ERG): A full-field ERG system (Celeris System, Diagnosis LLC, MA) was used to test the retinal function in *Bicdl1* WT and KI mice at different age groups (12-, 15-, and 17-19-month-old). After dark adaptation overnight for at least 16 hours, scotopic ERG recordings were performed under a dim red light on deeply anesthetized mice, as detailed previously [19-21]. Briefly, after pupil dilation and application of GenTeal gel (Novartis, East Hanover, NJ), both eyes were contacted with electrodes for full-field stimulation, producing two-channel recordings with 10 sweeps for each of three different light stimuli (0.01, 0.1, and 1 cd□s/m^2). Both the scotopic a-wave and scotopic b-wave were analyzed using Diagnosys Espion Software (Diagnosys, Lowell, MA). The photopic a-wave and b-wave were analyzed with the same system using two light stimuli (3 and 10 cd□s/m^2).

Statistical analysis: Data are presented as the mean±standard error of the mean (SEM). For all figures, groups of measurements were taken from distinct samples, rather than from repeated measurements. Sample sizes are included in each figure legend. Given the assumption of normal distribution of the data, comparisons between two groups were made using a two-tailed unpaired Student's *t*-test. One exception was the quantification of fundus spots, which was based on a non-continuous, ordinal scale and required non-parametric Mann-Whitney U testA linear regression analysis was done to test trends in fundus spot accumulation over time using age in months as the independent variable. In all comparisons, a p-value statistic of < 0.05 is considered significant. Graphs and statistical analysis were done using GraphPad Prism 9.4.1 (GraphPad Software, La Jolla, CA) and Microsoft Excel 16.63.1 (Microsoft, Redmond, WA).

RESULTS

Association between a Bicdl1 mutation and outer retinal thinning in a forward genetic screen in mice: Third-generation (G3) descendants in a pedigree of mice carrying mutations induced by ENU in G0 male mice [17] were screened for retinal phenotypes [18,19,21]. A pedigree containing 80 G3 mice was imaged using the OCT2 imaging system. TRT, ONL, and ORT were measured using ImageJ, as described before [19]. Automated meiotic mapping and evaluation of candidate mutations, respectively, by the Linkage Analyzer and Candidate Explorer software [17,27] led to the identification of a point mutation in *Bicdl1* (which we named "*bargain* allele" for easy reference). It was a substitution of guanine to adenine in coordinate 115,808,212 bp of the mouse genome (GRCm39), corresponding to the first nucleotide of *Bicdl1* intron 4. This was associated with a mild but highly significant decrease in ORT and TRT in four homozygous mice (Figure 1A,C; $p = 1.7 \times 10^{-6}$ and $p = 6 \times 10^{-6}$, respectively). The significance threshold after Bonferroni correction was $p < 0.0006$. Of note, the scatter plot showed a very tight distribution for the ORT parameter in the homozygous mice, compared to the TRT parameter (Figure 1B,D). Moreover, mice heterozygous (HET mice in Figure 1B,D) for the *Bicdl1* mutation did not show any difference in ORT or TRT compared to mice with no *Bicdl1* mutated alleles ("REF" mice in Figure 1B,D).

Outer retinal thinning in CRISPR-generated Bicdl1 KI mice: Little is known about the relevance and role of *Bicdl1* in retinal health. Therefore, to validate the effect of the *Bicdl1* mutation on ORT and TRT phenotypes on a clean background (with no other ENU-induced mutations) and to enable subsequent phenotypic and molecular studies, we generated *Bicdl1* KI mice having the same mutation that we identified in our forward genetics screen (a replacement allele – see Appendix 2). Ensembl, NCBI, and UniProt indicate the existence of several *Bicdl1* splice isoforms. In most of these, including the 577-aa canonical isoform, the effect of the KI mutation is predicted to be "probably null". There are two potential isoforms, predicted only by Ensembl (235-aa and 82-aa), that would not be affected by our mutation, but there is no published data supporting their existence. Bulk RNA seq data from the retina of the *Bicdl1* KI mice indicated a 75% decrease in *Bicdl1* transcript (Appendix 6), while expression of the housekeeping gene [28] RPP-30 was normal. This decrease in *Bicdl1* transcript in *Bicdl1* KI mice (despite the fact that there is only a point mutation in the DNA) suggests the activation of nonsense-mediated decay, supporting the conclusion that the mutation is indeed damaging.

A colony of *Bicdl1* KI mice was established, and OCT images were obtained at 3 weeks and 2, 4, 6, 9, 12, 15 months of age. Representative images are shown in Figure 2A-F. The ORT, TRT, and ONL were measured using ImageJ. For simplicity and labeling purposes, the terms KI or *Bicdl1* KI will be used to refer to homozygous *Bicdl1*$^{KI/KI}$ mice, while the terms Het and heterozygous will be used to refer to *Bicdl1*$^{KI/+}$ mice. We documented a statistically significant decrease in ORT (3-10%) in *Bicdl1* KI mice compared to the WT mice in all age groups (Figure 2G; $p < 0.01$ for each age group). Thinning of the ONL (3%) was first detected at 6 months of age (Figure 2H; $p = 0.02$). There was no difference in ORT, ONL, or TRT between female and male mice (Figure 2G-I). Heterozygous mice did not show any difference in ORT and ONL compared to WT mice (Appendix 7), confirming the data from the ENU mutagenesis screen (Figure 1B,D), indicating an autosomal recessive inheritance pattern, and strongly suggesting that the mutation causes a loss of function of the encoded protein.

To corroborate our findings of thinning in different retinal layers, retina sections were stained with H&E, and light microscopy images were obtained (Figure 3A-D). We demonstrated a statistically significant thinning of the ONL as measured by ONL thickness (up to 12%) and ONL nuclear count (up to 20%) in *Bicdl1* KI mice compared to WT mice at 9 months (Figure 3E,F) and 19 months of age (Figure 3G,H). To look specifically at the rod photoreceptor outer segments, we performed immunohistochemistry of retinal sections using a rhodopsin antibody (Figure 4A-D). Measurements using ImageJ revealed a significant decrease in the average thickness of the rod outer segments in *Bicdl1* KI mice compared to WT mice, both at 9 months (Figure 4E, 14% decrease, $p < 0.05$) and at 19 months of age (Figure 4F, 30% decrease, $p < 0.05$).

To determine whether the thinning of the ONL was due to apoptotic cell death, both a caspase-3 staining and a TUNEL assay were performed on retinal cross sections of 9 month and 19 month old mice. Interestingly, there were very few caspase-3 (Appendix 8) and TUNEL^{+} (Appendix 8) cells in both strains, and no significant difference in either assay.

Finally, analysis of the thickness of inner retinal layers (INL and GCC) using OCT and H&E did not show any significant differences between *Bicdl1* WT and KI mice (Appendix 9).

Increased number of fundus spots in Bicdl1 KI mice corresponding to subretinal microglia: Increased numbers of fundus spots are commonly seen in mouse models of retinal degeneration in aged mice. This finding often correlates with the presence of activated subretinal microglia [19-21,23,29].

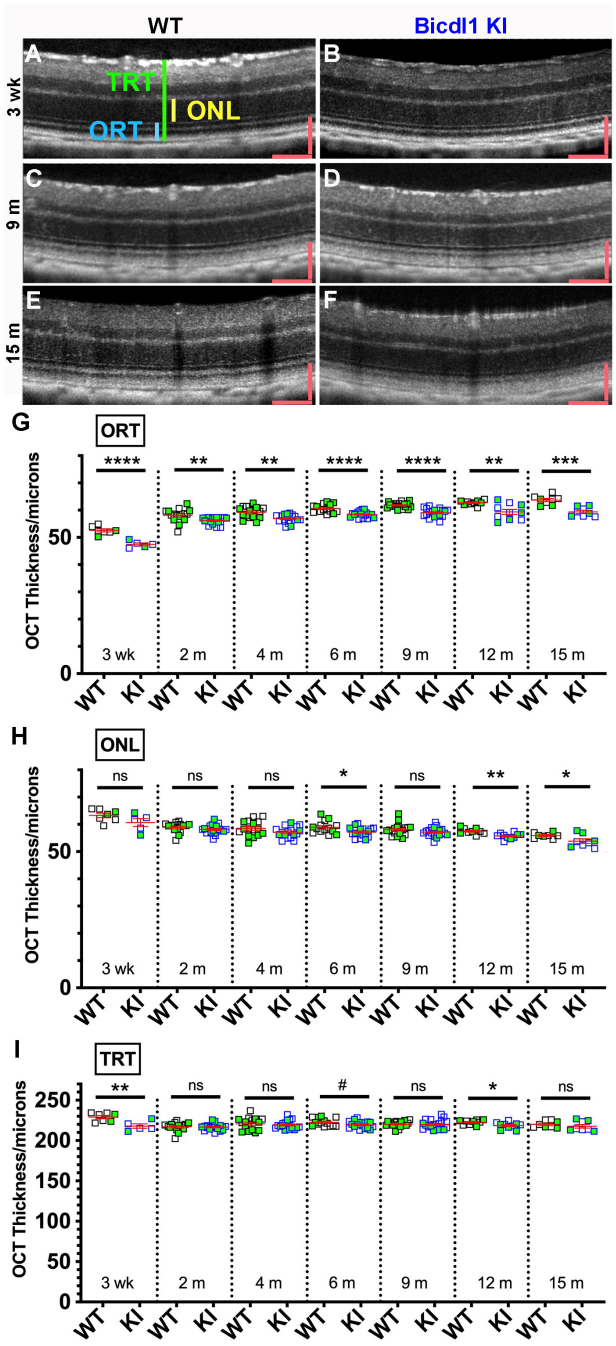

Figure 2. CRISPR-generated *Bicdl1* KI mice reconstitute the phenotype discovered in the mutagenesis screen. A *Bicdl1* KI mouse carrying a replacement allele for the bargain mutation was generated by CRISPR mutagenesis. **A**-**F**: Representative OCT images at 3 weeks, 9 months, and 15 months of age show decreased ORT. **G**-**I**: Quantification of ORT (**G**), ONL (**H**) and TRT (**I**) thicknesses at different ages (**G**, **H**, **I**; WT n = 7, KI n = 5 at 3-week-old, WT n = 16, KI n = 20 at 2-month-old, WT n = 16, KI n = 17 at 4-month-old, WT n = 14, KI n = 17 at 6-month-old, WT n = 19, KI n = 19 at 9-month-old, WT n = 9, KI n = 10 at 12-month-old, WT n = 8, KI n = 8 at 15-month-old) in *Bicdl1* WT and KI mice. A significant difference in ORT was observed between *Bicdl1* WT and KI mice at all time points. ONL thinning starts at 6 months of age. Black squares: WT mice, blue squares: *Bicdl1* KI mice, green-filled squares: male, open squares: female; green line: TRT, yellow line: ONL, blue line: ORT, ns: non-significant, #: $p < 0.1$, *: $p < 0.05$, **: $p < 0.01$, ***: $p < 0.001$, ****: $p < 0.0001$, scale bar: 100 µm.

To determine whether this was the case in *Bicdl1* KI mice, we took color fundus photographs at several time points (Figure 5A-J). A modified fundus spot scale was used for grading. Statistical analysis demonstrated a significant increase in the number of fundus spots at all time points after 2 months of age in the *Bicdl1* KI mice compared to WT, up to a tripling of the fundus spot grading by 15 months of age (Figure 5K). The trend analysis demonstrated a significant increase in fundus spots with age in *Bicdl1* KI mice but not in WT mice (Appendix 10).

In order to better characterize these fundus spots and understand their nature, we chose an eye with an asymmetric distribution of fundus spots and prepared an RPE flat mount, which we stained with the pan-microglia/macrophage marker Iba1 (Figure 6A-C). We found that the flat mount contained a similar distribution of Iba1$^+$ subretinal cells adhered to the RPE compared to the fundus spots, suggesting that the fundus spots correlated with activated subretinal microglia/macrophages. In a second experiment, we imaged eyes with fundus spots using both fundus photography and a Spectralis OCT. We then used the infrared images from the Spectralis OCT to overlap the vessels of both imaging modalities. This allowed us to "register" both images and look for an anatomical correlate for the fundus spots on OCT. We found that the fundus spots correlated with subretinal hyperreflective spots located just above the RPE (Appendix 11). Retina sections stained with anti-Iba1 antibodies revealed Iba1+ cells localizing to that same location in the subretinal space (immediately above the RPE) of *Bicdl1* KI but not WT mice (Appendix 11). We did not find any evidence for rosettes or true drusen. Finally, we studied the fundus photographs in more detail at early time points (2 and 4 months of age). Since there is a functional distinction between the superior and inferior retina in mice, including differences in photoreceptors, we decided to count fundus spots in each retina. As shown in Appendix 12, we found that the earliest increase in fundus spots in *Bicdl1* KI mice occurred in the superior hemiretina.

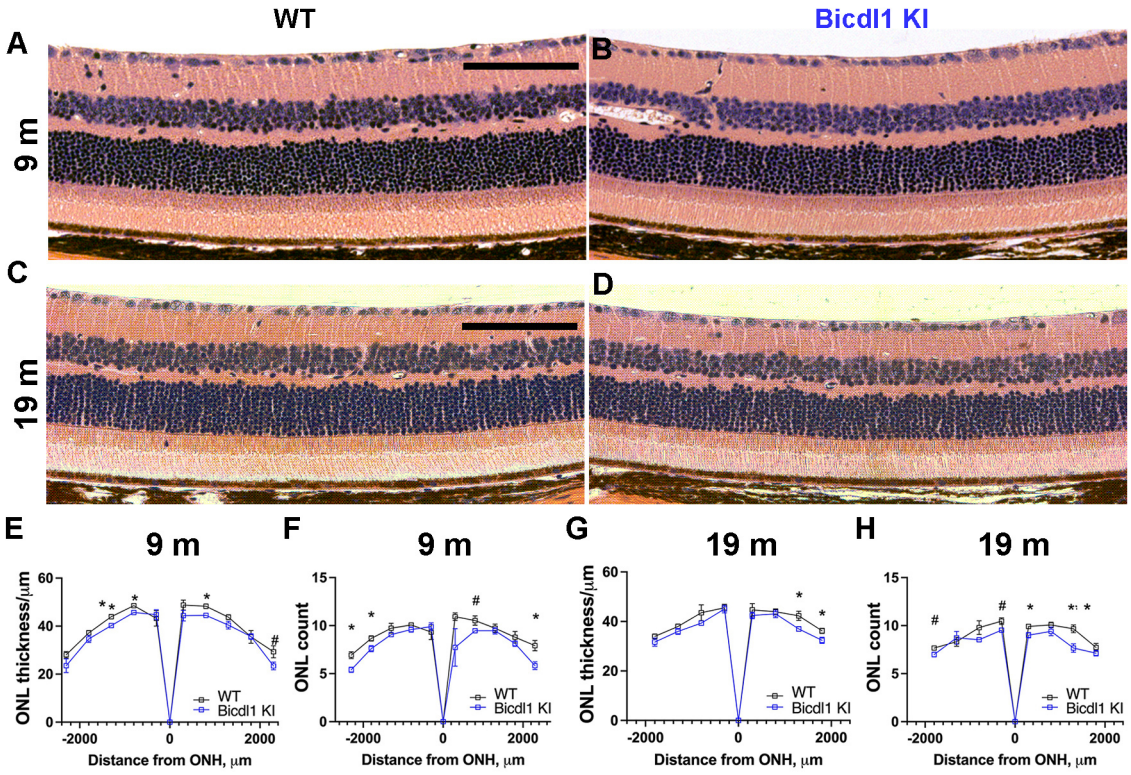

Figure 3. *Bicdl1* KI mice have a decreased number of photoreceptors and thinning of ONL in H&E-stained retina cross sections. **A**-**D**: Representative images of retina sections from 9- and 19-month-old mice stained with H&E. **E**-**H**: Quantification of ONL thicknesses (**E**, **G**) and ONL nuclei per column (photoreceptor cell body numbers; **F**, **H**) at 9 months of age (**E**, **F**; WT n = 4, KI n = 5) and 19 months of age (**G**, **H**; WT n = 5, KI n = 5). Measurements were taken at 500 µm intervals starting from 300 µm from the optic nerve head (ONH) on both sides. Black squares: WT mice, blue squares: *Bicdl1* KI mice. Data are shown as means ± SEM. # (non-significant trend): $p < 0.1$, *: $p < 0.05$, **: $p < 0.01$, Scale bar: 100 µm. ONL: outer nuclear layer.

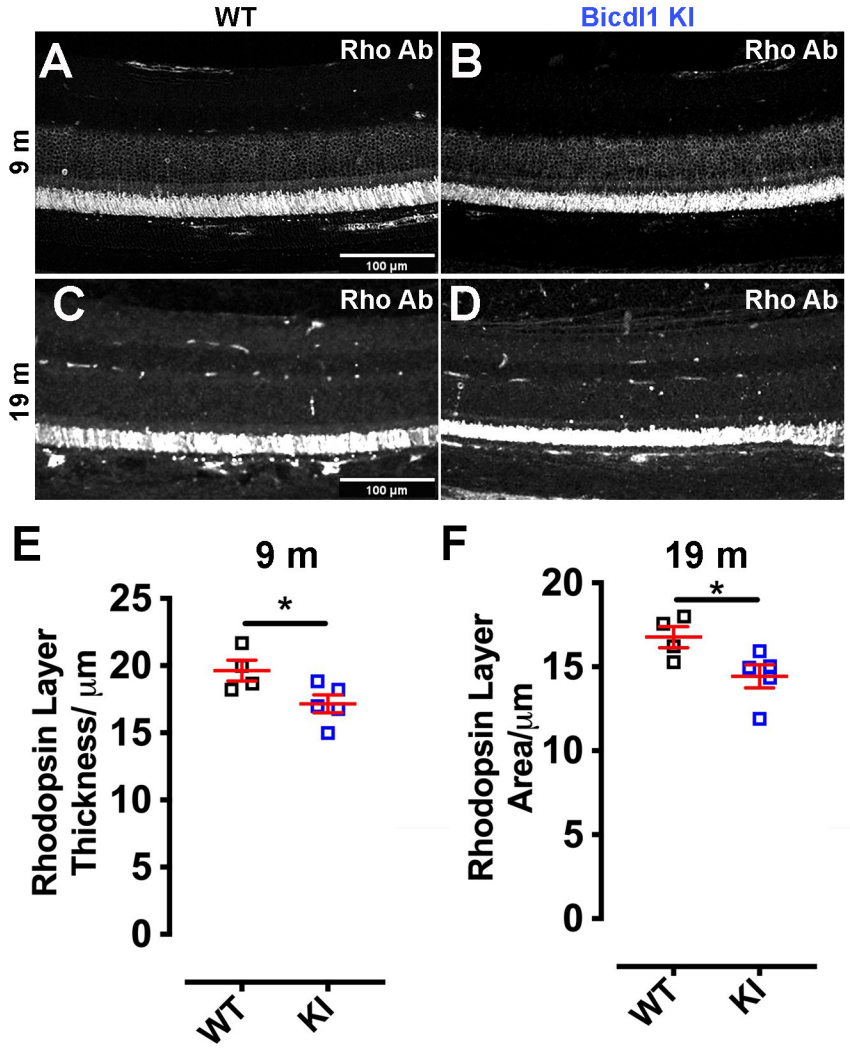

Figure 4. *Bicdl1* KI mice have significantly reduced average thickness of rod photoreceptor outer segment layer in retina cross sections, indicating shorter outer segments. **A**-**D**: Representative retinal sections from 9- and 19-month-old mice immunostained with anti-rhodopsin (white), labeling rod photoreceptor outer segments. Images were acquired using a 25x objective (NA 1.0). Quantification of the average thickness (area of staining divided by length of the imaged field) of the rhodopsin-stained outer segments in 9-month-old (E, WT n = 4, KI n = 5) and 19-month-old (F, WT n = 5, KI n = 5) mice is shown for *Bicdl1* WT and KI mice in the midperipheral zone. Rho Ab: Rhodopsin antibody, Black squares: WT mice, blue squares: *Bicdl1* KI mice. Data are shown as means ± SEM. *: $p < 0.05$, Scale bar: 100 µm.

RPE flat mounts were then prepared from 9-month-old mice and stained with anti-Iba1 (pan-microglial/macrophage marker) and anti-Tmem119 (specific for resident microglia) antibodies. We imaged paracentral and midperipheral areas in four quadrants on the RPE flat mounts. Representative images for the Iba1 staining, Tmem119 staining, and merged channels are shown in Figure 6D,E. Most of these cells were double-positive for Iba1 and Tmem119 staining (yellow cells in the merged-channel image). *Bicdl1* KI mice displayed a statistically significant increase in the number of $Iba1^+$ cells ($p = 0.03$, Figure 6F) and also $Tmem119^+$ cells ($p = 0.03$, Figure 6G) in the paracentral zone compared to WT mice. Of note, in addition to being positive for Tmem119, these cells were negative for CCR2 (Appendix 13). Negative controls for RPE flat mounts are shown in Appendix 14.

We also observed migration of inner retinal microglia to the outer retina, specifically to the photoreceptor outer segments (POS), exclusively in *Bicdl1* KI mice. These displaced microglia exhibited an activated ameboid morphology and stained positive for both Iba1 and TMEM119. In contrast, both WT and *Bicdl1* KI mice demonstrated the presence of Iba1+/TMEM119+ microglia in the inner plexiform layer (IPL) and outer plexiform layer (OPL). These cells

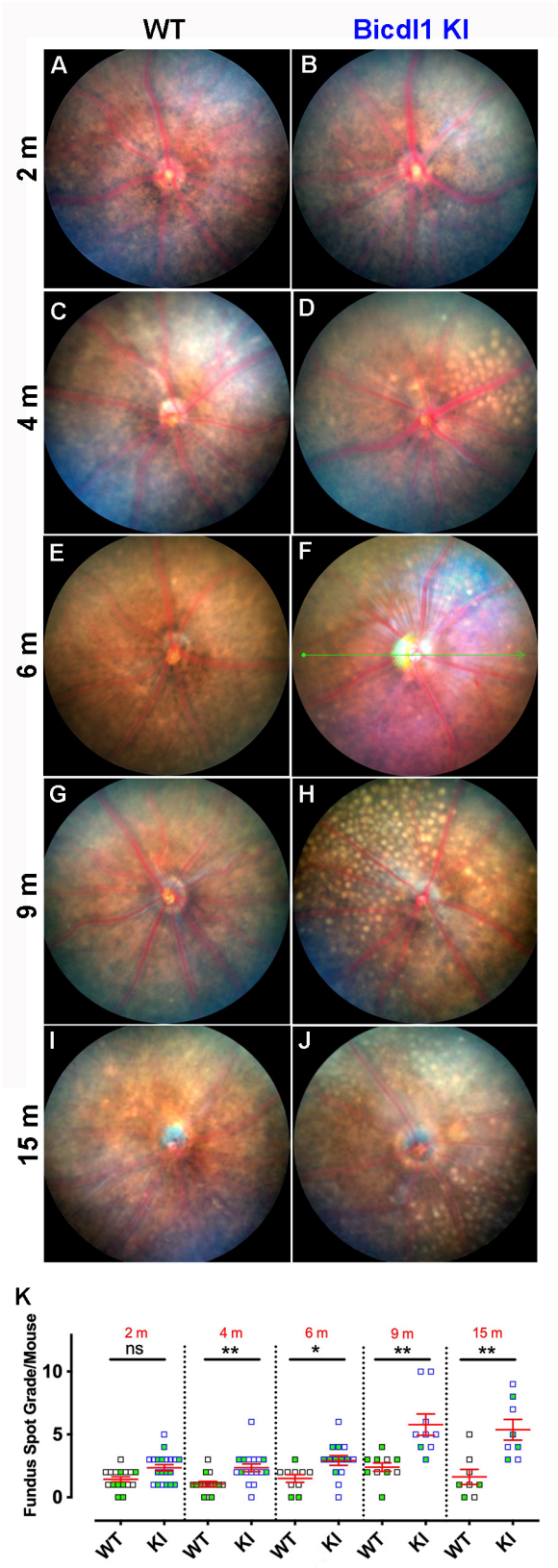

Figure 5. *Bicdl1* KI mice demonstrate an increased number of fundus spots compared to WT mice. **A**-**J**: Representative fundus images of WT and *Bicdl1* KI mice at 2, 4, 6, 9, and 15 months of age. **K**: Fundus spot grade per mouse at different age groups. There is a significant increase in the number of fundus spots in the *Bicdl1* KI mice at all time points after 2 months of age (2 m, WT n = 16, KI n = 20; 4 m, WT n = 15, KI n = 17; 6 m, WT n = 10, KI n = 14; 9 m, WT n = 10, KI n = 9; 15 m, WT n = 8, KI n = 8). The values represent the sum of the grading for the left and right eyes of each mouse. Black squares: WT mice, blue squares: *Bicdl1* KI mice, green filled square: male, open square: female. Data are shown as means ± SEM. ns: non-significant, *: $p < 0.05$, **: $p < 0.01$.

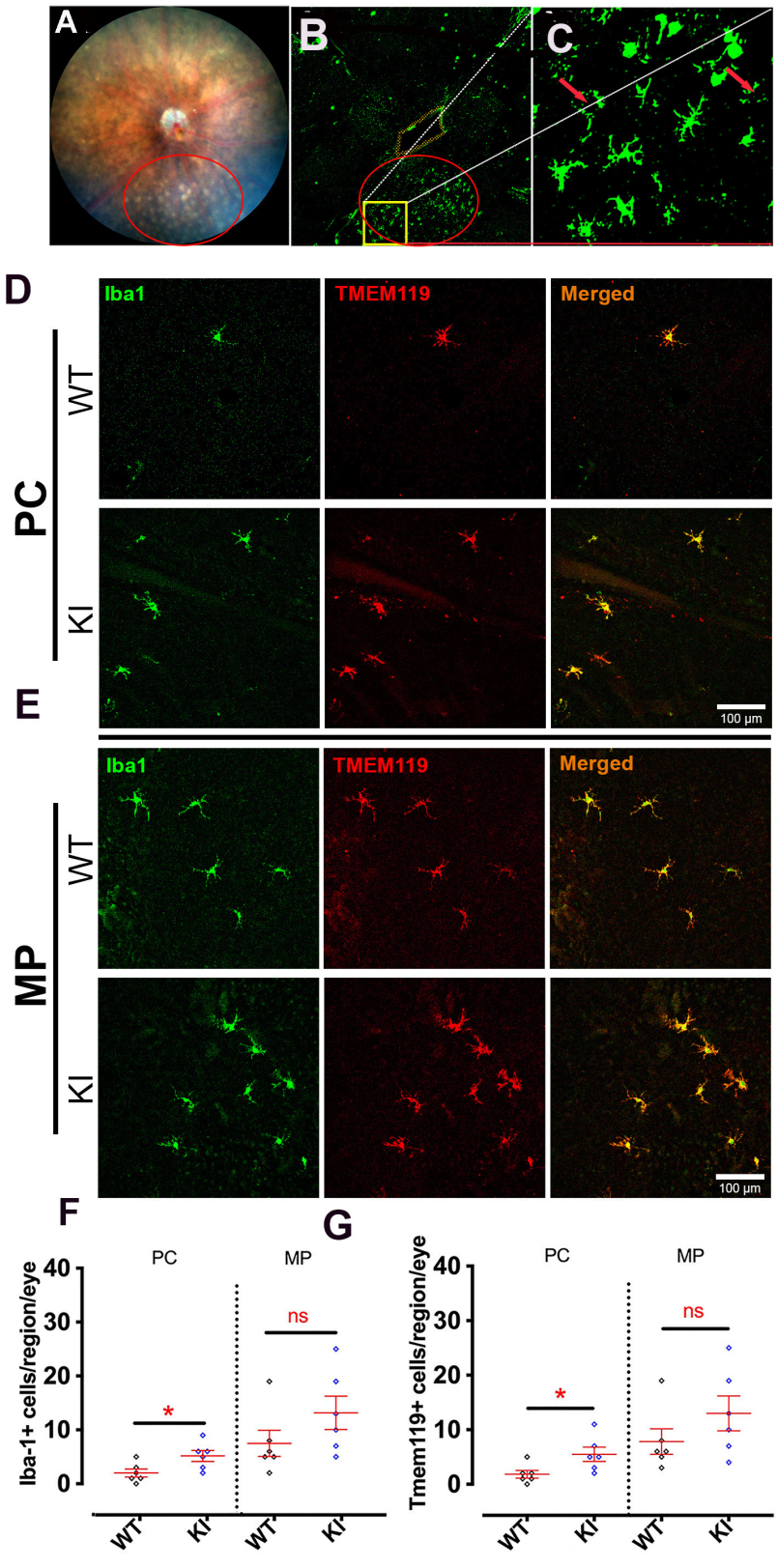

Figure 6. Subretinal microglia number is significantly increased in *Bicdl1* KI mice. **A**-**C**: Fundus spots appear to correspond to subretinal microglia. **A**: Fundus photo of mouse retina with a very asymmetric distribution of fundus spots. The majority of fundus spots are localized to a small area of the inferior retina (red oval). **B**: An RPE flat mount of the same eye demonstrates a similar distribution (red oval) of Iba1$^+$ microglia overlying the RPE. The orange, irregular dotted line highlights the cut on the posterior flat mount where the optic disc used to be. **C**: A magnified view of the yellow square in panel **B** shows Iba1+ cells with the typical morphology of both ramified and ameboid microglia. Some microglia lack cell bodies (red arrows), likely due to artifactual separation during flat-mount preparation. **D**, **E**: Representative RPE flat mounts images from 9-month-old WT and *Bicdl1* KI mice acquired with a 25× objective (NA 1.0) at the paracentral (**D**) and midperipheral (**E**) regions. Green cells are Iba1$^+$ microglia, red cells are Tmem119$^+$ microglia. **F**, **G**: Quantitative analysis shows increased subretinal Iba1$^+$ cells and Tmem119$^+$ cells in the paracentral region (**F**, **G**; WT, n = 6 eyes, KI, n = 6 eyes) in *Bicdl1* KI samples compared with WT samples. Measurements represent the average of all four quadrants per eye (**F**, **G**). PC: paracentral region (four quadrants); MP: midperipheral region (four quadrants). Black diamonds: WT mice, blue diamonds: *Bicdl1* KI mice, Data are shown as means ± SEM. ns: non-significant, *: $p < 0.05$, scale bar: 100 µm.

had a resting morphology, characterized by small cell bodies and long, branching extensions (Appendix 15).

Decreased retinal function in aging Bicdl1 KI mice: To determine if the outer retinal thickness changes observed in the *Bicdl1* KI mice led to functional consequences, we performed ERG on 12-, 15-, and 17-19-month-old mice (Figure 7). Scotopic ERG results did not reveal any differences at 12 months of age. However, at 15 months of age, there was a trend towards a decrease in a-wave amplitude ($p = 0.13$; Figure 7B), and at 17-19 months of age, there was a significant decrease in the a-wave amplitude both with the 0.1 (14% decrease, $p < 0.05$) and with the 1.0 cd□s/m^2 stimulus (18% decrease, $p < 0.01$). No consistent differences were detected in the b-wave amplitude at any time point (Figure 7C). This is concordant with the fact that the retinal degeneration in *Bicdl1* KI mice is relatively mild and primarily involves the outer retina. Of interest, we did not detect any consistent differences in the photopic ERG responses of *Bicdl1* KI mice (Appendix 16). Moreover, cone arrestin staining (Appendix 16) did not show evidence of decreased numbers of cones in the KI mice compared to the WT mice. The inner segment/outer segment layer did appear thinner in KI mice (consistent with the outer retinal thinning seen in OCT), but the cones did not show any gross dysmorphic features.

Enrichment of oxidative phosphorylation and protein synthesis pathways in photoreceptors in Bicdl1 KI mice: With the goal of better understanding the role of *Bicdl1* in the retina, we decided to analyze published scRNA-seq data from WT mice (C57BL/6J mice at P90, source data GEO:GSM7785354) [26], concentrating on rods and comparing cells showing high expression of *Bicdl1* to those with low expression. Pathway analysis of the differentially expressed genes revealed enrichment of genes in multiple mitochondrial and protein synthesis-related pathways, which together accounted for 12 of the top 25 pathways (Figure 8A,B). This analysis suggested that perturbations in mitochondrial and translation pathways may be associated with differential *Bicdl1* expression in rods.

To directly investigate gene expression changes resulting from *Bicdl1* loss of function, we conducted RNA sequencing of *Bicdl1* KI neuroretina and WT neuroretina in 9-week-old mice (Figure 8C,D). Although bulk RNA-seq yields gene expression data averaged across a population of cells, rods are by far the most common cell type in the retina, and *Bicdl1* is highly expressed in rods. We found that 16 of the top 25 affected pathways were shared between the scRNA-seq and bulk RNA-seq results, and in the same direction of change for every single one of those. That included the top 5 pathways. Both analyses showed significant effects of decreased expression of *Bicdl1* on four categories of pathways: energy metabolism-related pathways, protein synthesis-related pathways, oxidative stress and apoptosis-related pathways, and proliferation and regulation of transcription-related pathways (Figure 8, Appendix 4 and Appendix 5). We also found significant changes in the expression of several genes that might be associated with *Bicdl1* (Appendix 17), including regulators of energy metabolism in photoreceptors (*Ckb* and *Guk1*), antioxidant enzymes (*Gpx4, Sod1, Prdx2, Prdx4, Prdx5*), and mitophagy-related genes (*Fis1, Tomm6, Tomm7,* and *Tomm22*). Among 15 dynein subunit proteins, we found significantly increased expression levels of both isoforms of the dynein light chain roadblock genes *Dynlrb1* and *Dynlrb2* in *Bicdl1* KI mice versus WT mice [30]. Among the cargo adaptor proteins associated with the trans Golgi network [2,3,31,32], we found a significant increase in the expression of *Ap4s1* and *Ap1s1*, decreased expression of *Hook3*, and no significant change in the expression levels of *Bicd1, Bicd2, Hook2, and Ap3s1*. The expression levels of *Nudc*, which is involved in rhodopsin transport [33], and *Cfl1* were also increased (Appendix 17).

Decreased RPE mitochondria in Bicdl1 KI mice: Given the data suggesting an association of *Bicdl1* to oxidative phosphorylation, the reported expression of *Bicdl1* in RPE cells, and the fact that analysis of mitochondria is most reliable in RPE cells, we decided to perform an ultrastructural analysis of the RPE, including its mitochondria, in *Bicdl1* KI vs. WT mice.

Representative EM images are shown in Figure 9A-B. Measurements of EM images using ImageJ were analyzed using either each EM field as a replicate (Figure 9C, D) or using the average of each eye (Figure 9E, F) as a test replicate. Analysis per field suggested that *Bicdl1* KI RPE cells have thinner basal infoldings, a decrease in RPE thickness, and a decrease in the thickness of the Bruch's membrane-RPE complex (Figure 9C). It also suggested a highly significant decrease in the number of basal, apical, and total mitochondria in the RPE in *Bicdl1* KI mice (Figure 9D). Of note, when the analysis was repeated by mouse, rather than by EM field, the same trend for a reduction in RPE thickness parameters remained, but significance was lost (Figure 9E). Yet, the reduction in the number of mitochondria in *Bicdl1* KI RPE remained significant even after this stricter analysis (Figure 9F).

DISCUSSION

In this study, using a forward genetic approach, we identified an association between a *Bicdl1* mutation and outer retinal thinning. Ensembl, NCBI, and UniProt predict a 577-aa canonical isoform of *Bicdl1*. The predicted effect

of the *Bicdl1* mutation we identified is "probably null" due to a premature stop codon eliminating about half of the protein (Appendix 2). We decided to pursue this further by generating and characterizing a *Bicdl1* mutant mouse model of retinal degeneration for three reasons. First, using the NIH-supported eyeIntegration tool [34] we found that the expression level of *Bicdl1* mRNA in the human retina is highest in rods, cones, and RPE cells, followed by retinal ganglion cells and bipolar cells (Appendix 18). Second, the known role of *Bicdl1* in intracellular transport seems very relevant to photoreceptor and RPE homeostasis. Finally, the fact that the phenotypes detected in our OCT screen were distinct (mostly ORT thinning) and milder than those induced by other mutations we have described [18-21] could support the ability of the ENU-mutagenesis screen to detect non-redundant genes in retinal physiology, even with relatively minor changes on OCT. The retina has a remarkable ability to re-establish homeostasis due to an extensive redundancy

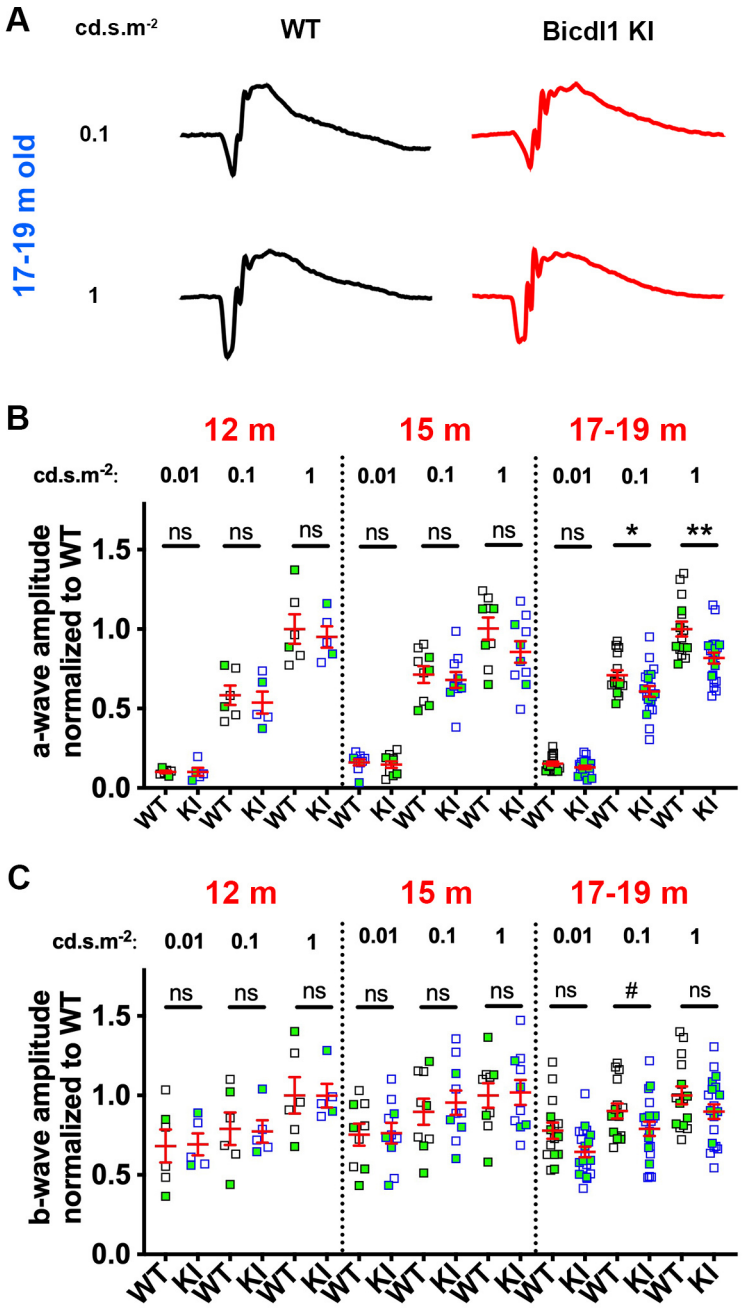

Figure 7. *Bicdl1* KI mice have decreased a-wave amplitude at 17-19 months of age. **A**: Representative ERG tracings of 17-19-month-old *Bicdl1* WT and KI mice are shown. **B**, **C**: Normalized a-wave (**B**, flash intensities 0.01, 0.1 and 1 cd□s/m^2) and b-wave amplitudes (**C**, flash intensities 0.01, 0.1, and 1 cd□s/m^2) from individual mice at 12 m (WT n = 6, KI n = 5), 15 m (WT n = 9, KI n = 10), and 17-19 m (WT n = 15, KI n = 19) are shown. A decreased a-wave is seen in aging *Bicdl1* KI mice (**B**). No significant difference was detected in b-wave (**C**). Black squares: WT mice, blue squares: *Bicdl1* KI mice, green filled squares: male, open squares: female. Data are shown as means ± SEM. ns: non-significant, #: $p < 0.1$, *: $p < 0.05$, **: $p < 0.01$.

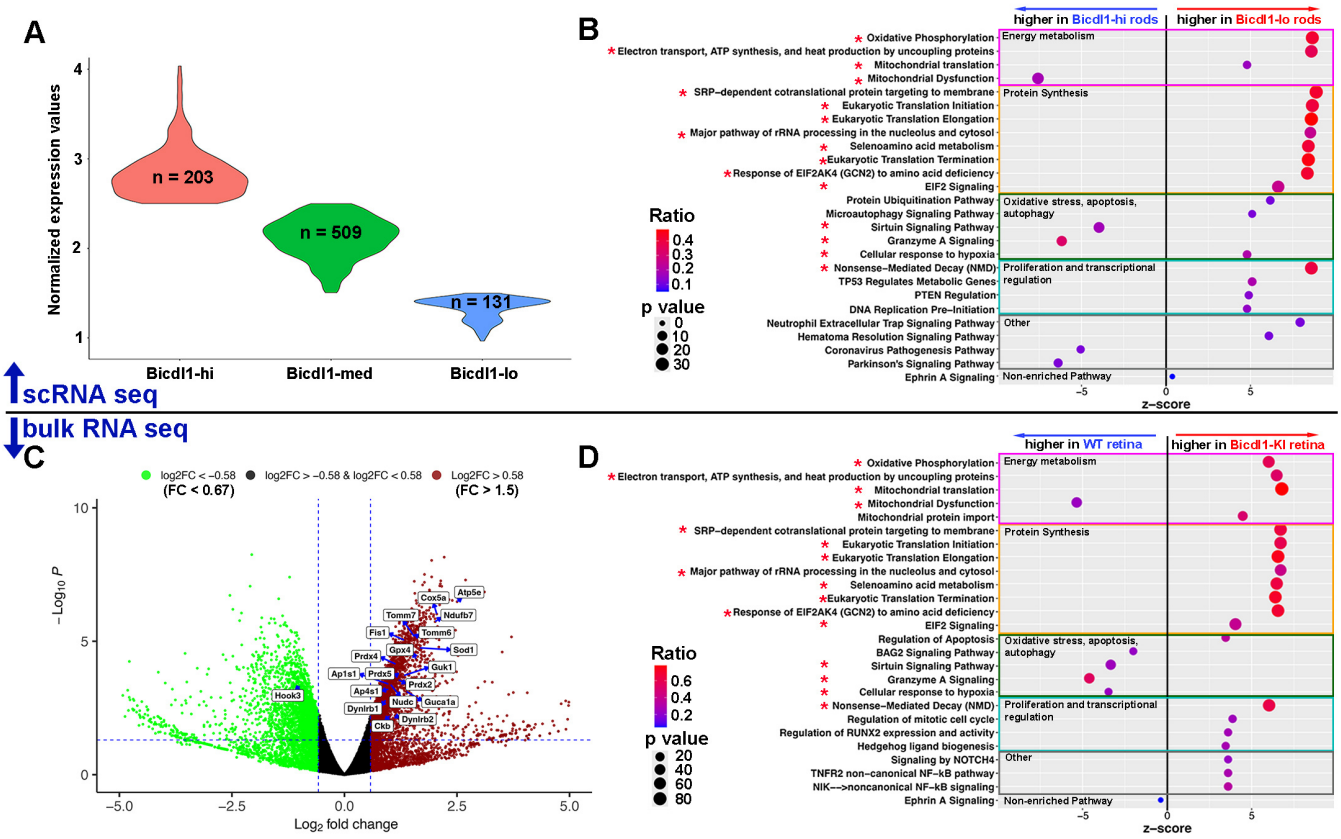

Figure 8. The pathway analyses generated from bulk RNA-seq and scRNA-seq data demonstrate significant changes in energy metabolism (purple frame), protein synthesis (yellow frame), oxidative stress/apoptosis/autophagy (green frame), and proliferation/transcription regulation (blue frame) related pathways. **A**: A violin plot shows the rod photoreceptor cells from the scRNA-seq data after splitting into high vs. medium vs. low expression of *Bicdl1*, and the total number of cells in each category. Expression levels for *Bicdl1* were defined as: *Bicdl1*-lo (expression >0 and <1.5), *Bicdl1*-med (expression 1.5-2.5), and *Bicdl1*-hi (expression >2.5). **B**: Top 25 pathways from scRNA-seq p90 rod photoreceptors comparing low vs. high expression of *Bicdl1* (*Bicdl1*-lo vs. *Bicdl1*-hi). **C**: A volcano plot shows expression levels of selected genes from bulk RNA-seq data. Green dots: genes with decreased level of expression, red dots: genes with increased level of expression. **D**: Top 25 pathways from bulk RNA-seq of retina samples from 9-week-old *Bicdl1* WT and KI mice comparing *Bicdl1* KI versus WT. *Bicdl1* WT, n = 4 pooled retinal samples; KI, n = 4 pooled retinal samples, with each pooled sample consisting of retinas from three individual mice. *: shared pathways between the scRNA-seq and bulk RNA-seq analysis.

in its signaling and metabolic pathways. Thus, even small changes in retinal anatomy and function caused by a mutation may point to special non-redundant genes, which could be potential “Achilles’ heels” for retinal cells. If the expression level of these genes is altered, even in the absence of a mutation, there may be important consequences for retinal health.

After generating the *Bicdl1* KI mouse model, we corroborated our mutagenesis screening data showing decreased ORT in OCT images. The difference was significant by 3 weeks of age, indicating that *Bicdl1* is important to retinal homeostasis even at an early age. Moreover, staining for rhodopsin antibody, which specifically stains the outer segments of rods, demonstrated a statistically significant thinning in the outer segment layer of *Bicdl1* KI mice. This is consistent with other retinal degeneration models, which are characterized by diminished or shorter outer segments [35-37]. With aging, we were also able to document mild thinning of the ONL, reflecting photoreceptor loss. Finally, ERG data from aging mice demonstrated a decreased a-wave amplitude in *Bicdl1* KI mice, indicating that the observed retinal changes resulted in deteriorated photoreceptor function. We did not see differences in either cone arrestin staining or photopic ERG responses, suggesting that the impact may be greater in rods vs. cone photoreceptors.

Intracellular transport is essential to maintaining cellular metabolic pathways, organization, and, ultimately, function. Various types of cargoes, including vesicles and organelles, are transported to their specific destinations

along microtubules by the motor proteins dynein and kinesin. Dynein specializes in retrograde transport (towards the minus end of microtubules), and kinesin is involved in anterograde transport (towards the plus end). While dynein and kinesin traverse microtubules in opposite directions, they cooperate to maintain the balance. Although the precise mechanism underlying this balance has not been fully understood, the net direction of intracellular transport may be regulated by several factors, including autoinhibition, selective binding of motors to the cargoes, and the force-generating power of the transport complex [2,38]. Typically, dynein exists in an autoinhibited state. The coiled-coil N-terminal of the Bicdl1 protein interacts with dynein and dynactin, thereby activating dynein [3,4]. Bicaudal D family of cargo adaptors has been shown to facilitate the transport of Rab6 vesicles by dynein [3,14,16]. Bicdl1 binds two dynein molecules. While in some situations Bicd2 can also bind two dynein molecules, Bicdl1 generates a stronger force, resulting in increased velocity. This feature of the Bicdl1 protein suggests it plays a decisive role in the post-Golgi transport by enhancing the rate

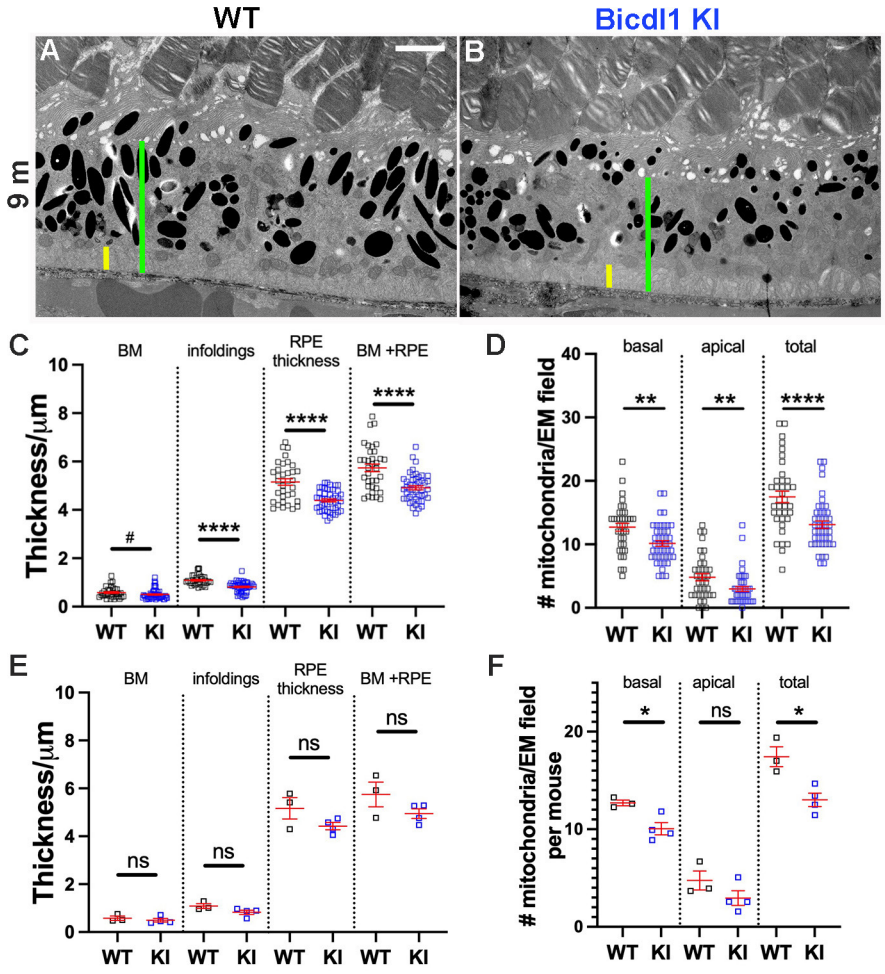

Figure 9. Ultrastructural analysis of RPE cells reveals abnormalities in *Bicdl1* KI mice. **A**, **B**: Representative EM images of RPE cells from 9-month-old *Bicdl1* KI (n = 4) and WT (n = 3) mice. **C**: Standardized and masked analysis demonstrates a decrease in the average thicknesses of RPE cells, basal infoldings, and the "bottom of BM to top of RPE" measurement. Ten to 13 EM fields were imaged per eye using a standardized and masked technique in which the whole sample was scanned, and three EM fields were skipped between each photographed EM field. **D**: Quantification of the average basal and apical mitochondria number in RPE cells in *Bicdl1* WT and KI mice are also presented as per EM field. *Bicdl1* KI mice have a decreased number of mitochondria in both the basal and apical regions of RPE cells. **E**, **F**: The same samples were also analyzed per mouse. There was still a trend towards decreased basal infoldings and RPE thickness, but this did not reach significance (**E**). Significance persisted for decreased basal and total mitochondria in KI mice (**F**). Green line: RPE cell body thickness (excluding the microvilli), yellow line: basal infoldings, black squares: WT mice, blue squares: *Bicdl1* KI mice, Data are shown as means ± SEM. ns: non-significant, *: $p < 0.05$, **: $p < 0.01$, ****: $p < 0.0001$. Scale bar: 2 µm. Images were captured at 2500x nominal magnification.

of retrograde transport of Rab6 vesicles [2,3,15,16,39-42]. During early embryogenesis in zebrafish, overexpression of *Bicdl1* results in the retention of Rab6 vesicles in the pericentrosomal region, suppressing the elongation of neural projections. The onset of neurite development in zebrafish embryos has been shown to be associated with a marked decrease in *Bicdl1* expression [3]. Similarly, overexpression of *Bicdl1* was shown to be associated with decreased transport of Rab6 vesicles to the neurites of hippocampal neurons (anterograde direction), resulting in the accumulation of these vesicles in the cell body [15]. In contrast to other neurons [43], in photoreceptors, the accumulation of vesicles in the perinuclear region represents accumulation near the plus end of microtubules. On the other hand, blocking expression of the zebrafish homolog of *Bicdl1* during embryogenesis resulted in a striking phenotype in which neural development was disrupted, and the eye failed to develop [3]. This indicates that the accumulation of Rab6 vesicles in the pericentrosomal region prior to the initiation of neuritogenesis may be essential for the accurate elongation of cellular projections. Yet, our *Bicdl1* KI mice appeared to undergo normal ocular development and grossly normal retinal development, suggesting that in mice, the role of *Bicdl1* during embryonic development may be at least partially compensated for by other molecules.

Still, the fact that ORT thinning could be detected as early as 3 weeks of age on OCT suggests that some of the effects of *Bicdl1* on the retina may indeed occur during development. The lack of evidence of increased apoptosis on TUNEL and Caspase staining also suggests that ongoing cell death is not a prominent feature of the mature retina, but it does not rule out earlier apoptosis. Early developmental analyses were not included in this study due to our late recognition of this feature of the clinical course, but will be included in our future mechanistic investigations. However, several clinical features did appear later in life (e.g., progressive accumulation of white/yellow fundus spots and decreased ERG function). These delayed features suggest a continued effect of *Bicdl1* deficiency beyond retinal development. Moreover, analysis of eyeIntegration data [34] and scRNA-seq data deposited by other groups[26] shows that *Bicdl1* expression is higher in mature human and mouse photoreceptors and RPE cells compared to developmental stages and to other cells in the retina (Appendix 18). Finally, eyeIntegration data also show that rod photoreceptors express [expression > 2 $\log_2$(CPM+1)] at least 5 cargo adaptor proteins (labeled as CA in Appendix 19), 2 dynein activators (labeled as DA in Appendix 19), and 13 additional proteins with both functions [2,31,32,44]. Our finding of an irreplaceable role for *Bicdl1* in mammalian retinal homeostasis is particularly interesting given the large number of available transport molecules, which might be expected to confer a high degree of redundancy [2,31,32,44].

Rab GTPases are vital for neurons and photoreceptors [13,43]. Sasaki et al have shown lytic photoreceptor death in Drosophila in Rab escort protein deficiency [45]. Specifically, Rab6 vesicles, which interact with Bicdl1, have been shown to be involved in polarized transport of molecules, including rhodopsin, in photoreceptors [46-51]. Our data support the hypothesis that *Bicdl1* dysfunction leads to a disruption in the minus-end-directed transport of these vesicles from the Golgi towards the basal body at the root of the connecting cilium, and ultimately towards the outer segments, resulting in thinning of the outer retina and impaired retinal function in *Bicdl1* KI mice. This finding underscores the essential role of intracellular trafficking in photoreceptors, highlighting the significant impact of mutations in the dynein system, which have been implicated in several retinal degenerative disorders [8,10,33,52,53].

We found a striking similarity between the results of the pathway analysis of scRNA-seq data (*Bicdl1*-lo vs. *Bicdl1*-hi rod photoreceptors) and our bulk RNA-seq data (*Bicdl1* KI vs. WT retina), despite the lack of cell-specific information in bulk RNA-seq data compared to scRNA-seq data. This implies that the effects of *Bicdl1* deficiency on the rod transcriptome are quite robust, in that they are detectable when averaged with signals across all retinal cell types. IPA revealed that in both datasets, out of the top 25 enriched pathways, four to five were related to energy metabolism and mitochondrial function (all indicating increased mitochondrial activity with decreased *Bicdl1* expression), and eight were related to the regulation of protein synthesis. Increased eIF2 signaling, as seen in the *Bicdl1* KI mice, is usually associated with a decrease in the rate of general protein synthesis, which is a common cellular response to increased energy needs, as the cell tries to conserve its energy [54]. Overall, an increase in the translation pathways and an increase in the eIF2 signaling pathway may represent a decrease in global protein synthesis but an increase in some translational pathways associated with low *Bicdl1* expression. Enrichment of energy metabolism pathways indicates an attempt by the retina to re-establish transport and to increase energy production for that purpose. To evaluate this, we looked at the expression levels of dynein subunit proteins, cargo adaptor proteins in the trans Golgi network, and regulator proteins of phototransduction in photoreceptors. We found increased expression of dynein roadblock light chain family genes, *Dynlrb1* and *Dynlrb2*. Dynlrb1 has been shown to interact with Rab6 family proteins and to participate in sensory neurite growth [55,56], like Bicdl1. The expression levels of

adaptor protein genes *Ap4s1* and *Ap1s1* were also increased, indicating a possible compensatory adjustment in the expression of adaptor proteins to re-establish homeostasis. Recently, Garner et al have shown the importance of Nudc and Cfl1 in the transport of rhodopsin to the outer segments [33]. We found that the *Bicdl1* KI retina has significantly increased expression levels of these two transcripts, pointing out another possible homeostatic response. Finally, our bulk RNA-seq data in *Bicdl1* KI neuroretina suggested an increased expression of *Guca1a*, a regulator of the phototransduction pathway in the outer segment, which may indicate the increased effort to maintain functionality, secondary to inadequate renewal of outer segments [57].

The development of ORT and ONL thinning in *Bicdl1* KI mice suggests that the compensatory responses are not entirely effective. Persistent transport defects may result in increased stress in the photoreceptors, in turn affecting other metabolic pathways, mainly energy metabolism. Photoreceptors use 80% of glucose in aerobic glycolysis for phototransduction and outer segment renewal, but oxidative phosphorylation is an important source of energy for visual metabolic pathways during scotopic conditions [58-61]. As photoreceptors rely on both glycolysis and oxidative phosphorylation to maintain their function, they can modulate their energy production under stress conditions [62,63]. Petit et al. have shown that loss of hexokinase-2 leads to increased expression of electron transport chain genes [63]. Here, we show that *Bicdl1* deficiency is strongly associated with increased activity in oxidative phosphorylation-related pathways. Moreover, we found increased expression of regulators of energy metabolism in photoreceptors such as *Ckb* and *Guk1* [64,65]. While this finding may at first seem counterintuitive, we hypothesize that the impaired intracellular transport caused by *Bicdl1* deficiency and the ensuing inadequate outer segment renewal may lead to a perceived need for additional energy and trigger a compensatory increase in the activity of signaling pathways involved in energy production (see Appendix 1) [58,62,63,66,67]. However, the compensatory increase in energy production may not be able to fully rescue the photoreceptor outer segments. It may perhaps even result in increased oxidative stress, autophagy, and mitophagy. Interestingly, we detected a significant increase in the expression levels of antioxidant enzymes (*Gpx4, Sod1, Prdx2, Prdx4, and Prdx5*), and mitophagy-related genes (*Fis1, Tomm6, Tomm7, Tomm22*). So, based on these data, the overall result of decreased *Bicdl1* expression appears to be increased need for energy secondary to impaired intracellular transport, which in turn leads to increased oxidative phosphorylation. We should emphasize that the observed transcriptomic changes indicate only association, not causation; the observed metabolic changes may reflect either a primary consequence of *Bicdl1* loss or a secondary compensatory response to photoreceptor stress.

Possible mechanisms explaining the photoreceptor pathology in *Bicdl1* KI mice include a primary transport defect or an effect of Bicdl1 on energy metabolism, as it has been shown that impaired aerobic glycolysis leads to shorter outer segments [60]. On the other hand, any deterioration in photoreceptor health may cause increased activity in energy metabolism and oxidative stress. Finally, it is possible that RPE cell function is affected by *Bicdl1* deficiency, and that the changes in photoreceptors are secondary to RPE dysfunction. Future in vitro work may allow us to explore these hypotheses. The *Bicdl1* KI mouse model may be useful in studying energy metabolism in photoreceptors.

Given these data, we hypothesize that a mutation in *Bicdl1* may result in impaired intracellular transport and impaired energy metabolism not only in the photoreceptors but also in RPE cells. Normal aging leads to RPE abnormalities, but exacerbated RPE senescence is thought to be an important pathogenic mechanism in many retinal degenerations, including age-related macular degeneration (AMD) [68-71]. RPE dysfunction in senescence is often associated with increased oxidative stress, altered numbers and morphology of mitochondria, shorter microvilli, diminished basal infoldings, and accumulation of subretinal deposits [68-70,72,73]. While further studies are needed to determine whether *Bicdl1* deficiency leads to increased RPE senescence, we did find fewer RPE mitochondria and a trend towards reduced RPE cell thickness in *Bicdl1* KI mice. These may be ultrastructural indicators of senescence and epithelial-mesenchymal transition (EMT) secondary to impaired oxygen metabolism [68,70,74]. Recently, Luo et al. pointed out the possible relationship between *Bicdl1* and EMT through the WNT pathway in colorectal cancer [75]. If there is indeed impaired RPE function, this could lead to inadequate photoreceptor outer segment homeostasis, which may be another reason for the shorter outer segments seen in *Bicdl1* KI photoreceptors. Of note, we did not perform any assays to test RPE function in *Bicdl1* KI eyes, so this remains a hypothesis to be tested.

Bicdl1 KI mice demonstrated mild ONL thinning on OCT (starting at 6 months of age), which was corroborated by both a decrease in ONL thickness and a decrease in the number of ONL nuclei in H&E-stained retina sections. The decrease in ONL nuclei suggests that there is an actual loss of photoreceptors. Also, pathway analysis of scRNA-seq and bulk RNA-seq data showed increased activity in the apoptosis-related pathways in *Bicdl1* KI mice. Interestingly,

a TUNEL assay revealed only minor levels of apoptotic cells in both *Bicdl1* WT and KI retina and no significant difference between the groups. These findings suggest a low level of apoptosis in *Bicdl1* KI mice, which would be consistent with the mild and slow degeneration we documented in this model.

An increased number of activated subretinal microglia is seen in AMD, retinal dystrophies, and multiple mouse models of retinal degeneration [23,29,76-81]. These microglia appear as yellow spots in fundus photographs [20,23,29]. Although less prominent than in some of the other models of retinal degeneration that we and others have characterized [19-21], we did detect an increased number of fundus spots in *Bicdl1* KI mice. Furthermore, we showed an increased subretinal microglia count in the paracentral region of RPE flat mounts. The lower magnitude of these changes compared to other models may correlate with the low level and slow progression of retinal degeneration in *Bicdl1* KI mice. It should be noted that while most of the published literature recognizes Tmem119 as a microglia-specific marker [77,82,83], it may underestimate the number of microglia in models with significant microglial activation due to decreased Tmem119 expression [84,85]. Also, while Tmem119 seems to distinguish microglia well from blood-derived macrophages, it has been shown to be expressed by other cell types, including dendritic cells in secondary lymphoid organs and brown adipose tissue, and in some acute injury models, in Müller glia [85,86]. Importantly, in addition to staining positive for the microglia-specific marker Tmem119, the subretinal microglia in *Bicdl1* KI mice were negative for the macrophage-specific marker CCR2. Thus, while the field of CNS immune cell markers remains in significant flux, rendering a definite conclusion difficult, it is very likely that the Iba1^{+} cells we detect are indeed microglia. Finally, some activated microglia may not have strongly adhered to the RPE, or even fully reached the subretinal space. In that case, they may partially or completely peel off from the RPE surface when the retina is removed during the preparation of RPE flat mounts. Thus, our counts likely underestimate the number of activated microglia. However, all samples were processed identically, and analyses were limited to genotype-matched comparisons to minimize this potential bias.

Two caveats regarding the magnitude of the changes observed in *Bicdl1* KI mice and the interpretation of their relevance should be noted. First, it is difficult to interpret the clinical significance of retinal structural changes and even harder to extrapolate the functional changes from animal models to humans. While we documented relatively mild anatomical changes on OCT, we did observe a 30% decrease in rod outer segment thickness and up to an 18% reduction in a-wave. Moreover, these changes may be amplified in long-lived organisms like humans. Second, while all three databases searched (Ensembl, NCBI, and UniProt) indicate the existence of several *Bicdl1* splice isoforms, including a 577-aa canonical isoform for which the effect of the KI mutation is predicted to be “probably null”, there are two additional isoforms predicted by Ensembl (235-aa and 82-aa), which would not be affected by our mutation. While supporting evidence for the existence of these transcripts is weaker than for the canonical isoform, if they do exist, their protein products may provide some *Bicdl1* functionality in *Bicdl1* KI mice. Nonetheless, the recessive retinal phenotype and *Bicdl1* transcript levels in *Bicdl1* KI mice indicate that the KI mutation is at least hypomorphic.

Another limitation of our study is that the *Bicdl1* KI model was developed on a C57BL/6J background. It should be considered that C57BL/6J mice have a mutation in nicotinamide nucleotide transhydrogenase (Nnt) that renders it nonfunctional. Nnt is important in mitochondrial metabolism. This, for example, makes B6J mice exhibit a more robust response to high-fat diets, including increased weight gain, and impaired glucose tolerance. On the other hand, other strains like C57BL/6N and Balb/c mice have known retinal degeneration.

In conclusion, this study not only reveals an essential role of *Bicdl1* in retinal health but also indicates a possible correlation between intracellular transport and energy metabolism. Although the importance of these two separate cellular pathways in multiple retinal diseases is well-documented, this study highlights a direct link between them through a cargo adaptor protein. By bringing this subject to light, we aim to pave the way for more research to understand the role of *Bicdl1* in photoreceptor health and the connection between intracellular transport and energy metabolism in photoreceptors and RPE cells. Expanding our understanding of the complex intracellular transport system in photoreceptors and RPE cells may help in the development of therapies for retinal degenerative diseases, including macular dystrophies, diabetes-induced retinal neurodegeneration, and macular degeneration [87-92].

Data statement: The data of this study are available from the corresponding author, Rafael Ufret-Vincenty, upon reasonable request.

APPENDIX 1. SUPPLEMENTARY FIGURE S1: PROTOCOL AND MAIN FINDINGS DIAGRAM.

To access the data, click or select the words “Appendix 1.” Forward genetics screening identified an association between a *Bicdl1* mutation and mild outer retinal thinning.

CRISPR-generated *Bicdl1* KI mice confirmed shorter outer segments (10-30% reduction depending on the assay and age) and mild photoreceptor loss, as well as a mild decrease in visual function with age. Transcriptomic analysis suggests increased oxidative phosphorylation and modulation of protein synthesis. (Created in BioRender. 2025) https://BioRender.com/sdz34j3)

APPENDIX 2. SUPPLEMENTARY FIGURE S2: GENERATION OF *BICDL1* KI MICE.

To access the data, click or select the words "Appendix 2." A) *Bargain* allele discovered in ENU mutagenesis screen. B) A replacement allele was generated by CRISPR-Cas9 mutagenesis, and sequencing confirmed a substitution of guanine by adenine (red rectangle), resulting in an early stop codon. An additional silent base substitution (purple arrow) was created to prevent "cut-back." C) Predicted null protein product for both *bargain* and the CRISPR-generated replacement allele: a frame-shifted protein product beginning after amino acid 306 of the protein and terminating after the inclusion of 8 aberrant amino acids.

APPENDIX 3. SUPPLEMENTARY TABLE S1: MATERIALS AND RESOURCES

To access the data, click or select the words "Appendix 3."

APPENDIX 4. SUPPLEMENTARY TABLE S2: PATHWAY ANALYSIS OF SCRNA-SEQ DATA. *BICDL1*-LO VS. *BICDL1*-HI

To access the data, click or select the words "Appendix 4."

APPENDIX 5. SUPPLEMENTARY TABLE S3: PATHWAY ANALYSIS OF BULK RNA-SEQ DATA. *BICDL1* KI VS. WT

To access the data, click or select the words "Appendix 5."

APPENDIX 6. SUPPLEMENTARY FIGURE S3: BULK RNA SEQUENCING DATA SHOW A 75% REDUCTION IN *BICDL1* TRANSCRIPT IN *BICDL1* KI MICE.

To access the data, click or select the words "Appendix 6." *Bicdl1* WT, n = 4 pooled retinal samples; KI, n = 4 pooled retinal samples, with each pooled sample consisting of retinas from three individual mice. ns: non-significant, *: $p < 0.05$.

APPENDIX 7. SUPPLEMENTARY FIGURE S4: THE *BICDL1* KI PHENOTYPE SHOWS AN AUTOSOMAL RECESSIVE INHERITANCE PATTERN.

To access the data, click or select the words "Appendix 7." Mice heterozygous (HET, n = 8) for the *Bicdl1* KI allele do not differ from WT (n = 9) mice in either ORT or ONL measurements of OCT images. Mice are 6 months old. Black squares: WT mice, green squares: *Bicdl1* HET mice, green filled squares: male gender, open squares: female gender, Data are shown as means ± SEM. ns: non-significant.

APPENDIX 8. SUPPLEMENTARY FIGURE S5: CASPASE-3 STAINING AND TUNEL STAINING OF RETINA SECTIONS DO NOT SHOW A SIGNIFICANT INCREASE IN APOPTOSIS IN *BICDL1* KI MICE.

To access the data, click or select the words "Appendix 8." A, B) Representative images of caspase-3 staining in retina sections of 19-month-old WT (A) and *Bicdl1* KI (B) . Caspase-3 positive cells are indicated by a red arrow. Scale bar = 20 µm. C, D) Representative images of TUNEL staining in 9-month-old WT (C) and *Bicdl1* KI (D) retina sections. TUNEL-positive cells are indicated by a white arrow. Scale bar = 100 µm. E,F) Quantification of caspase-3^+ (E) and $TUNEL^+$ (F) cells in retinas of 9- and 19-month-old mice demonstrates that there is a very low level of apoptosis, which was not found to be increased in *Bicdl1* KI mice. For caspase staining, n = 5 WT and 5 KI at 9 m, and n = 4 WT and 5 KI at 19 m. For TUNEL staining: n=5 WT and 5 KI at both 9 and 19 months of age. Black squares: WT mice, blue squares: *Bicdl1* KI mice. Data are shown as means ± SEM. ns: non-significant.

APPENDIX 9. SUPPLEMENTARY FIGURE S6: INNER RETINAL LAYER THICKNESS IS NOT AFFECTED IN *BICDL1* KI MICE.

To access the data, click or select the words "Appendix 9." Inner nuclear layer (INL: A, C, E) and ganglion cell complex (GCC: B, D, F) were measured on H&E (A-D) and OCT (E, F) in both *Bicdl1* KI mice (blue symbols) and WT mice (black symbols). All measurements were performed at two time points. H&E: 9 months (WT n = 5, KI n = 5) and 19 months (WT n = 5, KI n = 5); OCT: 6 months (WT n = 6, KI n = 6) and 12 months (WT n = 6, KI n = 6). No differences were seen in either parameter, in either H&E or OCT, at any time point. Data are shown as means ± SEM. ns: non-significant.

APPENDIX 10. SUPPLEMENTARY FIGURE S7: AGE-DEPENDENT TRENDS IN FUNDUS SPOT ACCUMULATION IN *BICDL1* KI MICE.

To access the data, click or select the words "Appendix 10." Trend analyses were performed on fundus spot grading of *Bicdl1* KI (total n = 68) and WT (total n = 59) mice at different ages (2-15 months of age). A) No significant trend in fundus spot grading is seen in WT mice with age. B) Linear regression analysis shows a statistically positive trend in fundus spot grading as the *Bicdl1* KI mice age.

APPENDIX 11. SUPPLEMENTARY FIGURE S8: FUNDUS SPOTS APPEAR TO CORRESPOND TO HYPERREFLECTIVE SPOTS OVERLYING THE RPE AND TO SUBRETINAL MICROGLIA ON THE APICAL SURFACE OF THE RPE.

To access the data, click or select the words "Appendix 11." A-E: A fundus photo showing fundus spots in a 15-month-old *Bicdl1* KI mouse (A) is overlayed on the Spectralis infrared image (B) accompanying the OCT in order to register the vessels and ensure the two images are at the same magnification and location. C) A magnified view of one of the fundus spots (red arrow) is shown. D) The OCT on the exact same location shows a hyperreflective spot overlying the RPE (red arrow). E) The same infrared image is shown separately in order to highlight that the vessels (red ovals) show the exact same magnification and orientation as the fundus photo. F) Another example of a fundus spot showing as a hyperreflective spot over the RPE. G,H) Representative images of Iba1 staining in 15-month-old WT (G) and *Bicdl1* KI (H) retina sections. Subretinal microglia located on the apical surface of the RPE are seen in the KI retina section (white arrow). Scale bar = 100 µm

APPENDIX 12. SUPPLEMENTARY FIGURE S9: FUNDUS SPOTS START ACCUMULATING IN THE SUPERIOR HEMIRETINA OF *BICDL1* KI FIRST.

To access the data, click or select the words "Appendix 12." We could detect a statistically significant increase in fundus spots in the superior hemiretina of *Bicdl1* KI compared to WT mice as early as 2 months of age. n = 16 WT and 20 KI at 2 m, and n = 15 WT and 17 KI at 4 m. At these early time points, there was still no significant increase in fundus spots in the inferior retina.

APPENDIX 13. SUPPLEMENTARY FIGURE S10: CCR2 STAINING OF RPE FLAT MOUNTS SHOWS NO INFILTRATING MONOCYTE-DERIVED MACROPHAGES IN WT AND *BICDL1* KI MICE.

To access the data, click or select the words "Appendix 13." Dual immunofluorescence staining of RPE flat mounts from 15-month-old WT and *Bicdl1* KI mice using antibodies against Iba1 and CCR2. *Bicdl1* KI retinas display marked Iba1$^+$ microglial activation in the absence of CCR2 signal, whereas WT retinas show baseline Iba1$^+$ resting microglia with no detectable CCR2 expression. Scale bar = 100 µm.

APPENDIX 14. SUPPLEMENTARY FIGURE S11: NEGATIVE CONTROLS FOR RPE FLAT MOUNT FROM WT AND *BICDL1* KI MICE.

To access the data, click or select the words "Appendix 14." RPE flat mounts from 15-month-old WT and *Bicdl1* KI mice were incubated with secondary antibodies alone (without primary antibodies) to serve as negative controls for the dual immunofluorescence experiments. Images were acquired using identical microscope settings as experimental groups, confirming the absence of nonspecific background signal in both channels. Scale bar = 100 µm.

APPENDIX 15. SUPPLEMENTARY FIGURE S12: *BICDL1 KI* MICE DISPLAY ACTIVATED MICROGLIA IN THE OUTER RETINA.

To access the data, click or select the words "Appendix 15." Dual immunofluorescence staining of retina flat mounts from 15-month-old WT and *Bicdl1* KI mice using antibodies against Iba1 and TMEM119. Confocal images were acquired at the level of the inner plexiform layer (IPL), outer plexiform layer (OPL), and photoreceptor outer segments (POS). Activated microglia accumulation in the POS was observed exclusively in *Bicdl1* KI mice. Scale bar = 100 µm.

APPENDIX 16. SUPPLEMENTARY FIGURE S13: PHOTOPIC ERG RESPONSES AND CONE ARRESTIN STAINING ARE NOT ALTERED IN *BICDL1* KI MICE.

To access the data, click or select the words "Appendix 16." A, B) Normalized a-wave (A) and b-wave (B) amplitudes at flash intensities of 3 and 10 cd□s/m^2 were measured in individual mice under light-adapted conditions at 12 m (WT n = 6, KI n = 5), 15 m (WT n = 9, KI n = 10), and 17-19 m (WT n = 15, KI n = 19). C) Cone arrestin$^+$ cells were counted in the central, paracentral, and peripheral regions of the retina in both *Bicdl1* KI mice and WT mice at 19 m (WT n = 5, KI

n = 5). No consistent differences in photopic ERG responses or number of cone arrestin-stained cells were observed between WT and KI mice. D) Representative cone arrestin-stained cells are shown for WT and KI mice with inner/outer segments marked. Scale bar in panel D = 50 µm. Black squares: WT mice, blue squares: *Bicdl1* KI mice, green filled squares: male, open squares: female. ns: non-significant, *: $p < 0.05$.

APPENDIX 17. SUPPLEMENTARY TABLE S4: EXPRESSION LEVELS OF SELECTED GENES IN BULK RNA SEQUENCING DATA

To access the data, click or select the words "Appendix 17."

APPENDIX 18. SUPPLEMENTARY FIGURE S14: NIH-SUPPORTED EYEINTEGRATION DATA ANALYSIS REVEALS THE EXPRESSION LEVELS OF *BICDL1* DURING DEVELOPMENT (A) AND IN MATURE STAGES (B) OF HUMAN RETINA.

To access the data, click or select the words "Appendix 18."

APPENDIX 19. SUPPLEMENTARY FIGURE S15: EXPRESSION LEVELS OF SELECTED CARGO ADAPTOR PROTEIN GENES (CA) AND DYNEIN ACTIVATING PROTEIN GENES (DA) WITH AN EXPRESSION LEVEL > 2 LOG2(CPM+1) IN ROD PHOTORECEPTORS ACCORDING TO AN ANALYSIS OF EYE INTEGRATION DATA.

To access the data, click or select the words "Appendix 19."

ACKNOWLEDGEMENTS

Funding sources: This study was supported by NEI grants-1R01EY033181 and 1R21EY036238 (R.L.U-V.), National Eye Institute; Visual Science Core Grant P30 EY030413; RPB Challenge Grant (UTSW Ophthalmology), VanSickle Family Foundation Grant (R.L.U-V.); David M. Crowley Foundation Grant (R.L.U-V.) and NIH grant R01 AI125581 (B.A.B.). Our research was also supported in part by the Josephine Long Biddle Chair in Age-Related Macular Degeneration Research, the Lillian and James Cain Endowment in Vision Loss, the Anne Marie and Thomas B. Walker Jr. Fund for Research on Macular Degeneration of the Retina, and the Department of Ophthalmology at UTSW. This manuscript is the result of funding in whole or in part by the National Institute of Health (NIH) Public Access Policy. Through acceptance of this federal funding, NIH has been given a right to make this manuscript publicly available in PubMed Central upon the Official Date of Publication, as defined by NIH. **Other:** The authors want to acknowledge the statistical analysis help from Dr. Yaomin Xu, PhD, Associate Professor in the Department of Health Data Science & Biostatistics at the Peter O'Donnell Jr. School of Public Health, UT Southwestern Medical Center, and the contributions of the Molecular Histo Pathology Core, the Electron Microscopy Core, and the Transgenic Core at UTSW Medical Center. Author Contributions R.L.U-V.: conceptualization, formal analysis, funding acquisition, methodology, data curation, supervision, project administration, visualization, writing-review and editing; B.B.: conceptualization, funding acquisition; G.U-Y.: formal analysis, investigation, project administration, methodology, data curation, validation, visualization, writing-original draft; D.C.K.: formal analysis, investigation, writing-review and editing; B.A.: formal analysis, investigation, supervision, writing-review and editing; Y.G-H.: funding acquisition; E.T.: investigation; S.S.: investigation; T.Y.: investigation; S.Y.: investigation; S.L.: investigation; A.K.: formal analysis; C.X.: formal analysis; E.M.Y.M.: writing-review and editing. G.U-Y. and R.L.U-V. had full access to all the data in the study and takes full responsibility for the integrity of the data and the accuracy of the data analysis. Dr. Bogale Aredo (Bogale.Aredo@UTSouthwestern.edu), Dr. Bruce A. Beutler, MD (Bruce.Beutler@UTSouthwestern.edu) and Rafael Ufret-Vincenty (Rafael.Ufret-Vincenty@UTSouthwestern.edu) are co-corresponding authors for this paper. Portions of this study were presented at the ARVO 2025 Annual meeting. **Declaration of interest:** None **Funding:** This study was supported by NEI grants-1R01EY033181 and 1R21EY036238 (R.L.U-V.), National Eye Institute; Visual Science Core Grant P30 EY030413; RPB Challenge Grant (UTSW Ophthalmology), VanSickle Family Foundation Grant (R.L.U-V.); David M. Crowley Foundation Grant (R.L.U-V.) and NIH grant R01 AI125581 (B.A.B.). Our research was also supported in part by the Josephine Long Biddle Chair in Age-Related Macular Degeneration Research, the Lillian and James Cain Endowment in Vision Loss, the Anne Marie and Thomas B. Walker Jr. Fund for Research on Macular Degeneration of the Retina, and the Department of Ophthalmology at UTSW. Commercial Relationships Disclosure: None

REFERENCES

1. Walenta JH, Didier AJ, Liu X, Krämer H. The Golgi-associated hook3 protein is a member of a novel family of microtubule-binding proteins. J Cell Biol 2001; 152:923-34. [PMID: 11238449].

2. Canty JT, Yildiz A. Activation and Regulation of Cytoplasmic Dynein. Trends Biochem Sci 2020; 45:440-53. [PMID: 32311337].

3. Schlager MA, Kapitein LC, Grigoriev I, Burzynski GM, Wulf PS, Keijzer N, de Graaff E, Fukuda M, Shepherd IT, Akhmanova A, Hoogenraad CC. Pericentrosomal targeting of Rab6 secretory vesicles by Bicaudal-D-related protein 1 (BICDR-1) regulates neuritogenesis. EMBO J 2010; 29:1637-51. [PMID: 20360680].

4. Gallisà-Suñé N, Sànchez-Fernàndez-de-Landa P, Zimmermann F, Serna M, Regué L, Paz J, Llorca O, Lüders J, Roig J. BICD2 phosphorylation regulates dynein function and centrosome separation in G2 and M. Nat Commun 2023; 14:2434-[PMID: 37105961].

5. Feng D, Chen Z, Yang K, Miao S, Xu B, Kang Y, Xie H, Zhao C. The cytoplasmic tail of rhodopsin triggers rapid rod degeneration in kinesin-2 mutants. J Biol Chem 2017; 292:17375-86. [PMID: 28855254].

6. Jia B, Wang CG, Chen H, Zhou XB, Qian K, Chen C, Xu LX, Fu JL. The effect of cytoplasmic dynein on the development and functional maintenance of retinal photoreceptor cells. Eur Rev Med Pharmacol Sci 2021; 25:6539-47. [PMID: 34787856].

7. Kennedy B, Malicki J. What drives cell morphogenesis: a look inside the vertebrate photoreceptor. Dev Dyn 2009; 238:2115-38. [PMID: 19582864].

8. Krock BL, Mills-Henry I, Perkins BD. Retrograde intraflagellar transport by cytoplasmic dynein-2 is required for outer segment extension in vertebrate photoreceptors but not arrestin translocation. Invest Ophthalmol Vis Sci 2009; 50:5463-71. [PMID: 19474410].

9. Malhotra H, Barnes CL, Calvert PD. Functional compartmentalization of photoreceptor neurons. Pflugers Arch 2021; 473:1493-516. [PMID: 33880652].

10. Zhang J, Jing M, Li P, Sun L, Pi X, Jiang N, Zhu KK, Li H, Li J, Wang M, Zhang J, Liu M, Mu H, Hu Y, Cui X. Knockout of DLIC1 leads to retinal cone degeneration via disturbing Rab8 transport in zebrafish. Biochim Biophys Acta Mol Basis Dis 2023; 1869:166645[PMID: 36682603].

11. Storrie B, Micaroni M, Morgan GP, Jones N, Kamykowski JA, Wilkins N, Pan TH, Marsh BJ. Electron tomography reveals Rab6 is essential to the trafficking of trans-Golgi clathrin and COPI-coated vesicles and the maintenance of Golgi cisternal number. Traffic 2012; 13:727-44. [PMID: 22335553].

12. Liu S, Storrie B. How Rab proteins determine Golgi structure. Int Rev Cell Mol Biol 2015; 315:1-22. [PMID: 25708460].

13. Brault JB, Bardin S, Lampic M, Carpentieri JA, Coquand L, Penisson M, Lachuer H, Victoria GS, Baloul S, El Marjou F, Boncompain G, Miserey-Lenkei S, Belvindrah R, Fraisier V, Francis F, Perez F, Goud B, Baffet AD. RAB6 and dynein drive post-Golgi apical transport to prevent neuronal progenitor delamination. EMBO Rep 2022; 23:e54605[PMID: 35979738].

14. Matanis T, Akhmanova A, Wulf P, Del Nery E, Weide T, Stepanova T, Galjart N, Grosveld F, Goud B, De Zeeuw CI, Barnekow A, Hoogenraad CC. Bicaudal-D regulates COPI-independent Golgi-ER transport by recruiting the dynein-dynactin motor complex. Nat Cell Biol 2002; 4:986-92. [PMID: 12447383].

15. Schlager MA, Serra-Marques A, Grigoriev I, Gumy LF, Esteves da Silva M, Wulf PS, Akhmanova A, Hoogenraad CC. Bicaudal d family adaptor proteins control the velocity of Dynein-based movements. Cell Rep 2014; 8:1248-56. [PMID: 25176647].

16. Reck-Peterson SL, Redwine WB, Vale RD, Carter AP. The cytoplasmic dynein transport machinery and its many cargoes. Nat Rev Mol Cell Biol 2018; 19:382-98. [PMID: 29662141].

17. Wang T, Zhan X, Bu CH, Lyon S, Pratt D, Hildebrand S, Choi JH, Zhang Z, Zeng M, Wang KW, Turer E, Chen Z, Zhang D, Yue T, Wang Y, Shi H, Wang J, Sun L, SoRelle J, McAlpine W, Hutchins N, Zhan X, Fina M, Gobert R, Quan J, Kreutzer M, Arnett S, Hawkins K, Leach A, Tate C, Daniel C, Reyna C, Prince L, Davis S, Purrington J, Bearden R, Weatherly J, White D, Russell J, Sun Q, Tang M, Li X, Scott L, Moresco EM, McInerney GM, Karlsson Hedestam GB, Xie Y, Beutler B. Real-time resolution of point mutations that cause phenovariance in mice. Proc Natl Acad Sci U S A 2015; 112:E440-9. [PMID: 25605905].

18. Chen B, Aredo B, Ding Y, Zhong X, Zhu Y, Zhao CX, Kumar A, Xing C, Gautron L, Lyon S, Russell J, Li X, Tang M, Anderton P, Ludwig S, Moresco EMY, Beutler B, Ufret-Vincenty RL. Forward genetic analysis using OCT screening identifies *Sfxn3* mutations leading to progressive outer retinal degeneration in mice. Proc Natl Acad Sci U S A 2020; 117:12931-42. [PMID: 32457148].

19. Ufret-Vincenty RL, Kirman DC, Ulker-Yilmazer G, Aredo B, Shrestha S, Turpin E, Yuksel S, Zegeye Y, Ludwig S, Moresco EMY, He YG, Beutler B. Nonredundant Role of Leishmanolysin-Like (Lmln) Zinc-Metallopeptidase in Retinal Homeostasis. Am J Ophthalmol 2025; 269:147-60. [PMID: 39209209].

20. Yuksel S, Aredo B, Zegeye Y, Zhao CX, Tang M, Li X, Hulleman JD, Gautron L, Ludwig S, Moresco EMY, Butovich IA, Beutler BA, Ufret-Vincenty RL. Forward genetic screening using fundus spot scale identifies an essential role for Lipe in murine retinal homeostasis. Commun Biol 2023; 6:533-[PMID: 37198396].

21. Zegeye Y, Aredo B, Yuksel S, Kirman DC, Kumar A, Chen B, Turpin E, Shresta S, He YG, Gautron L, Tang M, Li X, DiCesare SM, Hulleman JD, Xing C, Ludwig S, Moresco EMY, Beutler BA, Ufret-Vincenty RL. E3 ubiquitin ligase Herc3 deficiency leads to accumulation of subretinal microglia and retinal neurodegeneration. Sci Rep 2024; 14:3010-[PMID: 38321224].

22. Chen B, Aredo B, Zhu Y, Ding Y, Xin-Zhao C, Ufret-Vincenty RL. A Mouse Model of Retinal Recovery From Photo-Oxidative/Photo-Inflammatory Injury: Nrf2, SOD1, DJ-1, and Parkin Are Not Essential to Recovery. Invest Ophthalmol Vis Sci 2019; 60:1165-74. [PMID: 30908580].

23. Aredo B, Zhang K, Chen X, Wang CX, Li T, Ufret-Vincenty RL. Differences in the distribution, phenotype and gene expression of subretinal microglia/macrophages in

C57BL/6N (Crb1 rd8/rd8) versus C57BL6/J (Crb1 wt/wt) mice. J Neuroinflammation 2015; 12:6-[PMID: 25588310].

24. Gavrieli Y, Sherman Y, Ben-Sasson SA. Identification of programmed cell death in situ via specific labeling of nuclear DNA fragmentation. J Cell Biol 1992; 119:493-501. [PMID: 1400587].

25. Krenacs L, Krenacs T, Stelkovics E, Raffeld M. Heat-induced antigen retrieval for immunohistochemical reactions in routinely processed paraffin sections. Methods Mol Biol 2010; 588:103-19. [PMID: 20012825].

26. Li J, Choi J, Cheng X, Ma J, Pema S, Sanes JR, Mardon G, Frankfort BJ, Tran NM, Li Y, Chen R. Comprehensive single-cell atlas of the mouse retina. bioarch. 2024.

27. Wang T, Bu CH, Hildebrand S, Jia G, Siggs OM, Lyon S, Pratt D, Scott L, Russell J, Ludwig S, Murray AR, Moresco EMY, Beutler B. Probability of phenotypically detectable protein damage by ENU-induced mutations in the Mutagenetix database. Nat Commun 2018; 9:441-[PMID: 29382827].

28. Molomjamts M, Ingolfsland EC. Identification of reference genes for the normalization of retinal mRNA expression by RT-qPCR in oxygen induced retinopathy, anemia, and erythropoietin administration. PLoS One 2023; 18:e0284764[PMID: 37098032].

29. Luhmann UF, Robbie S, Munro PM, Barker SE, Duran Y, Luong V, Fitzke FW, Bainbridge JW, Ali RR, MacLaren RE. The drusenlike phenotype in aging Ccl2-knockout mice is caused by an accelerated accumulation of swollen autofluorescent subretinal macrophages. Invest Ophthalmol Vis Sci 2009; 50:5934-43. [PMID: 19578022].

30. Dahl TM, Baehr W. Review: Cytoplasmic dynein motors in photoreceptors. Mol Vis 2021; 27:506-17. [PMID: 34526758].

31. Guo Y, Sirkis DW, Schekman R. Protein sorting at the trans-Golgi network. Annu Rev Cell Dev Biol 2014; 30:169-206. [PMID: 25150009].

32. Park SY, Guo X. Adaptor protein complexes and intracellular transport. Biosci Rep 2014; 34:e00123[PMID: 24975939].

33. Garner MA, Hubbard MG, Boitet ER, Hubbard ST, Gade A, Ying G, Jones BW, Baehr W, Gross AK. NUDC is critical for rod photoreceptor function, maintenance, and survival. FASEB J 2024; 38:e23518[PMID: 38441532].

34. Bryan JM, Fufa TD, Bharti K, Brooks BP, Hufnagel RB, McGaughey DM. Identifying core biological processes distinguishing human eye tissues with precise systems-level gene expression analyses and weighted correlation networks. Hum Mol Genet 2018; 27:3325-39. [PMID: 30239781].

35. Moye AR, Singh R, Kimler VA, Dilan TL, Munezero D, Saravanan T, Goldberg AFX, Ramamurthy V. ARL2BP, a protein linked to retinitis pigmentosa, is needed for normal photoreceptor cilia doublets and outer segment structure. Mol Biol Cell 2018; 29:1590-8. [PMID: 29718757].

36. Westfall JE, Hoyt C, Liu Q, Hsiao YC, Pierce EA, Page-McCaw PS, Ferland RJ. Retinal degeneration and failure of photoreceptor outer segment formation in mice with targeted deletion of the Joubert syndrome gene, Ahi1. J Neurosci 2010; 30:8759-68. [PMID: 20592197].

37. Gao J, Cheon K, Nusinowitz S, Liu Q, Bei D, Atkins K, Azimi A, Daiger SP, Farber DB, Heckenlively JR, Pierce EA, Sullivan LS, Zuo J. Progressive photoreceptor degeneration, outer segment dysplasia, and rhodopsin mislocalization in mice with targeted disruption of the retinitis pigmentosa-1 (Rp1) gene. Proc Natl Acad Sci U S A 2002; 99:5698-703. [PMID: 11960024].

38. Franker MA, Hoogenraad CC. Microtubule-based transport - basic mechanisms, traffic rules and role in neurological pathogenesis. J Cell Sci 2013; 126:2319-29. [PMID: 23729742].

39. Elshenawy MM, Canty JT, Oster L, Ferro LS, Zhou Z, Blanchard SC, Yildiz A. Cargo adaptors regulate stepping and force generation of mammalian dynein-dynactin. Nat Chem Biol 2019; 15:1093-101. [PMID: 31501589].

40. Urnavicius L, Lau CK, Elshenawy MM, Morales-Rios E, Motz C, Yildiz A, Carter AP. Cryo-EM shows how dynactin recruits two dyneins for faster movement. Nature 2018; 554:202-6. [PMID: 29420470].

41. Grotjahn DA, Chowdhury S, Xu Y, McKenney RJ, Schroer TA, Lander GC. Cryo-electron tomography reveals that dynactin recruits a team of dyneins for processive motility. Nat Struct Mol Biol 2018; 25:203-7. [PMID: 29416113].

42. Chaaban S, Carter AP. Structure of dynein-dynactin on microtubules shows tandem adaptor binding. Nature 2022; 610:212-6. [PMID: 36071160].

43. Zhang Y, Kunii M, Taniguchi M, Yoshimura SI, Harada A. Rab6-Mediated Polarized Transport of Synaptic Vesicle Precursors Is Essential for the Establishment of Neuronal Polarity and Brain Formation. J Neurosci 2024; 44:e2334232024[PMID: 38830762].

44. Olenick MA, Holzbaur ELF. Dynein activators and adaptors at a glance. J Cell Sci 2019; 132:jcs227132[PMID: 30877148].

45. Sasaki S, Satoh R, Satoh T, Satoh AK. Lytic photoreceptor cell death caused by Rab escort protein deficiency in Drosophila. FEBS Lett 2025; 599:2598-611. [PMID: 40325959].

46. Shetty KM, Kurada P, O'Tousa JE. Rab6 regulation of rhodopsin transport in Drosophila. J Biol Chem 1998; 273:20425-30. [PMID: 9685396].

47. Deretic D, Papermaster DS. Rab6 is associated with a compartment that transports rhodopsin from the trans-Golgi to the site of rod outer segment disk formation in frog retinal photoreceptors. J Cell Sci 1993; 106:803-13. [PMID: 8308063].

48. Wang J, Deretic D. Molecular complexes that direct rhodopsin transport to primary cilia. Prog Retin Eye Res 2014; 38:1-19. [PMID: 24135424].

49. Fogerty J, Denton K, Perkins BD. Mutations in the Dynein1 Complex are Permissible for Basal Body Migration in Photoreceptors but Alter Rab6 Localization. Adv Exp Med Biol 2016; 854:209-15. [PMID: 26427413].

50. Satoh T, Nakamura Y, Satoh AK. Rab6 functions in polarized transport in Drosophila photoreceptors. Fly (Austin) 2016; 10:123-7. [PMID: 27116570].

51. Iwanami N, Nakamura Y, Satoh T, Liu Z, Satoh AK. Rab6 Is Required for Multiple Apical Transport Pathways but Not the Basolateral Transport Pathway in Drosophila Photoreceptors. PLoS Genet 2016; 12:e1005828[PMID: 26890939].

52. Dahl TM, Reed M, Gerstner CD, Baehr W. Conditional Deletion of Cytoplasmic Dynein Heavy Chain in Postnatal Photoreceptors. Invest Ophthalmol Vis Sci 2021; 62:23-[PMID: 34807236].

53. Vig A, Poulter JA, Ottaviani D, Tavares E, Toropova K, Tracewska AM, Mollica A, Kang J, Kehelwathugoda O, Paton T, Maynes JT, Wheway G, Arno G, Khan KN, McKibbin M, Toomes C, Ali M, Di Scipio M, Li S, Ellingford J, Black G, Webster A, Rydzanicz M, Stawiński P, Płoski R, Vincent A, Cheetham ME, Inglehearn CF, Roberts A, Heon E. Genomics England Research Consortium. DYNC2H1 hypomorphic or retina-predominant variants cause nonsyndromic retinal degeneration. Genet Med 2020; 22:2041-51. [PMID: 32753734].

54. Stępkowski TM, Linke V, Stadnik D, Zakrzewski M, Zawada AE, Serwa RA, Chacinska A. Temporal alterations of the nascent proteome in response to mitochondrial stress. Cell Rep 2024; 43:114803[PMID: 39361503].

55. Terenzio M, Di Pizio A, Rishal I, Marvaldi L, Di Matteo P, Kawaguchi R, Coppola G, Schiavo G, Fisher EMC, Fainzilber M. DYNLRB1 is essential for dynein mediated transport and neuronal survival. Neurobiol Dis 2020; 140:104816[PMID: 32088381].

56. Wanschers B, van de Vorstenbosch R, Wijers M, Wieringa B, King SM, Fransen J. Rab6 family proteins interact with the dynein light chain protein DYNLRB1. Cell Motil Cytoskeleton 2008; 65:183-96. [PMID: 18044744].

57. Biasi A, Marino V, Dal Cortivo G, Maltese PE, Modarelli AM, Bertelli M, Colombo L, Dell'Orco D. A Novel *GUCA1A* Variant Associated with Cone Dystrophy Alters cGMP Signaling in Photoreceptors by Strongly Interacting with and Hyperactivating Retinal Guanylate Cyclase. Int J Mol Sci 2021; 22:10809-[PMID: 34639157].

58. Lin MK, Kim SH, Zhang L, Tsai YT, Tsang SH. Rod metabolic demand drives progression in retinopathies. Taiwan J Ophthalmol 2015; 5:105-8. [PMID: 29018679].

59. Hanna J, David LA, Touahri Y, Fleming T, Screaton RA, Schuurmans C. Beyond Genetics: The Role of Metabolism in Photoreceptor Survival, Development and Repair. Front Cell Dev Biol 2022; 10:887764[PMID: 35663397].

60. Chinchore Y, Begaj T, Wu D, Drokhlyansky E, Cepko CL. Glycolytic reliance promotes anabolism in photoreceptors. Elife 2017; 6:6-[PMID: 28598329].

61. Pan WW, Wubben TJ, Besirli CG. Photoreceptor metabolic reprogramming: current understanding and therapeutic implications. Commun Biol 2021; 4:245-[PMID: 33627778].

62. Wubben TJ, Pawar M, Smith A, Toolan K, Hager H, Besirli CG. Photoreceptor metabolic reprogramming provides survival advantage in acute stress while causing chronic degeneration. Sci Rep 2017; 7:17863-[PMID: 29259242].

63. Petit L, Ma S, Cipi J, Cheng SY, Zieger M, Hay N, Punzo C. Aerobic Glycolysis Is Essential for Normal Rod Function and Controls Secondary Cone Death in Retinitis Pigmentosa. Cell Rep 2018; 23:2629-42. [PMID: 29847794].

64. Wimberg H, Janssen-Bienhold U, Koch KW. Control of the Nucleotide Cycle in Photoreceptor Cell Extracts by Retinal Degeneration Protein 3. Front Mol Neurosci 2018; 11:52-[PMID: 29515371].

65. Hemmer W, Riesinger I, Wallimann T, Eppenberger HM, Quest AF. Brain-type creatine kinase in photoreceptor cell outer segments: role of a phosphocreatine circuit in outer segment energy metabolism and phototransduction. J Cell Sci 1993; 106:671-83. [PMID: 8282772].

66. Eckmiller MS. Defective cone photoreceptor cytoskeleton, alignment, feedback, and energetics can lead to energy depletion in macular degeneration. Prog Retin Eye Res 2004; 23:495-522. [PMID: 15302348].

67. Wong-Riley MT, Besharse JC. The kinesin superfamily protein KIF17: one protein with many functions. Biomol Concepts 2012; 3:267-82. [PMID: 23762210].

68. Tong Y, Zhang Z, Wang S. Role of Mitochondria in Retinal Pigment Epithelial Aging and Degeneration. Front Aging 2022; 3:926627[PMID: 35912040].

69. Skowronska-Krawczyk D, Finnemann SC, Grant MB, Held K, Hu Z, Lu YR, Malek G, Sennlaub F, Sparrow J, D'Amore PA. Features that distinguish age-related macular degeneration from aging. Exp Eye Res 2025; 254:110303[PMID: 39986366].

70. Malek G, Campisi J, Kitazawa K, Webster C, Lakkaraju A, Skowronska-Krawczyk D. Does senescence play a role in age-related macular degeneration? Exp Eye Res 2022; 225:109254[PMID: 36150544].

71. Berson EL, Adamian M. Ultrastructural findings in an autopsy eye from a patient with Usher's syndrome type II. Am J Ophthalmol 1992; 114:748-57. [PMID: 1463045].

72. Singh K, Jin Y, Hu MW, Palazzo I, Cano M, Hoang T, Bhutto I, Wang S, Sinha D, Blackshaw S, Qian J, Handa JT. Cigarette smoke and biological age induce degenerative heterogeneity in retinal pigment epithelium. bioarch. 2025

73. Brown EE, DeWeerd AJ, Ildefonso CJ, Lewin AS, Ash JD. Mitochondrial oxidative stress in the retinal pigment epithelium (RPE) led to metabolic dysfunction in both the RPE and retinal photoreceptors. Redox Biol 2019; 24:101201[PMID: 31039480].

74. Lefevere E, Toft-Kehler AK, Vohra R, Kolko M, Moons L, Van Hove I. Mitochondrial dysfunction underlying outer retinal diseases. Mitochondrion 2017; 36:66-76. [PMID: 28365408].

75. Luo H, Luo J, Ding N, Zhang T, He Y. BICDL1 Predicts Poor Prognosis and is Correlated with Methylation and Immune

Infiltration in Colorectal Cancer. Pharmgenomics Pers Med 2023; 16:1109-26. [PMID: 38149287].

76. Gupta N, Brown KE, Milam AH. Activated microglia in human retinitis pigmentosa, late-onset retinal degeneration, and age-related macular degeneration. Exp Eye Res 2003; 76:463-71. [PMID: 12634111].

77. Yu C, Lad EM, Mathew R, Shiraki N, Littleton S, Chen Y, Hou J, Schlepckow K, Degan S, Chew L, Amason J, Kalnitsky J, Bowes Rickman C, Proia AD, Colonna M, Haass C, Saban DR. Microglia at sites of atrophy restrict the progression of retinal degeneration via galectin-3 and Trem2. J Exp Med 2024; 221:e20231011[PMID: 38289348].

78. Altmann C, Schmidt MHH. The Role of Microglia in Diabetic Retinopathy: Inflammation, Microvasculature Defects and Neurodegeneration. Int J Mol Sci 2018; 19:110-[PMID: 29301251].

79. Zhao L, Zabel MK, Wang X, Ma W, Shah P, Fariss RN, Qian H, Parkhurst CN, Gan WB, Wong WT. Microglial phagocytosis of living photoreceptors contributes to inherited retinal degeneration. EMBO Mol Med 2015; 7:1179-97. [PMID: 26139610].

80. Zhong X, Aredo B, Ding Y, Zhang K, Zhao CX, Ufret-Vincenty RL. Fundus Camera-Delivered Light-Induced Retinal Degeneration in Mice With the RPE65 Leu450Met Variant is Associated With Oxidative Stress and Apoptosis. Invest Ophthalmol Vis Sci 2016; 57:5558-67. [PMID: 27768794].

81. Aredo B, Li T, Chen X, Zhang K, Wang CX, Gou D, Zhao B, He Y, Ufret-Vincenty RL. A chimeric Cfh transgene leads to increased retinal oxidative stress, inflammation, and accumulation of activated subretinal microglia in mice. Invest Ophthalmol Vis Sci 2015; 56:3427-40. [PMID: 26030099].

82. Satoh J, Kino Y, Asahina N, Takitani M, Miyoshi J, Ishida T, Saito Y. TMEM119 marks a subset of microglia in the human brain. Neuropathology 2016; 36:39-49. [PMID: 26250788].

83. Bennett ML, Bennett FC, Liddelow SA, Ajami B, Zamanian JL, Fernhoff NB, Mulinyawe SB, Bohlen CJ, Adil A, Tucker A, Weissman IL, Chang EF, Li G, Grant GA, Hayden Gephart MG, Barres BA. New tools for studying microglia in the mouse and human CNS. Proc Natl Acad Sci U S A 2016; 113:E1738-46. [PMID: 26884166].

84. Masuda T, Amann L, Sankowski R, Staszewski O, Lenz M, D Errico P, Snaidero N, Costa Jordão MJ, Böttcher C, Kierdorf K, Jung S, Priller J, Misgeld T, Vlachos A, Meyer-Luehmann M, Knobeloch KP, Prinz M. Novel Hexb-based tools for studying microglia in the CNS. Nat Immunol 2020; 21:802-15. [PMID: 32541832].

85. Vankriekelsvenne E, Chrzanowski U, Manzhula K, Greiner T, Wree A, Hawlitschka A, Llovera G, Zhan J, Joost S, Schmitz C, Ponsaerts P, Amor S, Nutma E, Kipp M, Kaddatz H. Transmembrane protein 119 is neither a specific nor a reliable marker for microglia. Glia 2022; 70:1170-90. [PMID: 35246882].

86. Su N, März S, Plagemann T, Cao J, Schnittler HJ, Eter N, Heiduschka P. Occurrence of Transmembrane Protein 119 in the Retina is Not Restricted to the Microglia: An Immunohistochemical Study. Transl Vis Sci Technol 2019; 8:29-[PMID: 31853425].

87. Baptista FI, Pinto MJ, Elvas F, Martins T, Almeida RD, Ambrósio AF. Diabetes induces changes in KIF1A, KIF5B and dynein distribution in the rat retina: implications for axonal transport. Exp Eye Res 2014; 127:91-103. [PMID: 25064602].

88. Cho HD, Nhàn NTT, Zhou C, Tu K, Nguyen T, Sarich NA, Yamada KH. KIF13B mediates VEGFR2 recycling to modulate vascular permeability. Cell Mol Life Sci 2023; 80:91-[PMID: 36928770].

89. Esteve-Rudd J, Hazim RA, Diemer T, Paniagua AE, Volland S, Umapathy A, Williams DS. Defective phagosome motility and degradation in cell nonautonomous RPE pathogenesis of a dominant macular degeneration. Proc Natl Acad Sci U S A 2018; 115:5468-73. [PMID: 29735674].

90. Jiang M, Esteve-Rudd J, Lopes VS, Diemer T, Lillo C, Rump A, Williams DS. Microtubule motors transport phagosomes in the RPE, and lack of KLC1 leads to AMD-like pathogenesis. J Cell Biol 2015; 210:595-611. [PMID: 26261180].

91. Song H, Bush RA, Vijayasarathy C, Fariss RN, Kjellstrom S, Sieving PA. Transgenic expression of constitutively active RAC1 disrupts mouse rod morphogenesis. Invest Ophthalmol Vis Sci 2014; 55:2659-68. [PMID: 24651551].

92. Waters SB, Zhou C, Nguyen T, Zelkha R, Lee H, Kazlauskas A, Rosenblatt MI, Malik AB, Yamada KH. VEGFR2 Trafficking by KIF13B Is a Novel Therapeutic Target for Wet Age-Related Macular Degeneration. Invest Ophthalmol Vis Sci 2021; 62:5-[PMID: 33533881].

Articles are provided courtesy of Emory University and The Abraham J. & Phyllis Katz Foundation. The print version of this article was created on 10 July 2026. This reflects all typographical corrections and errata to the article through that date. Details of any changes may be found in the online version of the article.